Development of luminescence dating methods in tectonically active settings: dating seismic related fanglomerates in alluvial fans located in Coachella Valley, southern California

by

Nina Ataee

B.S., University of Tehran, 2010
M.S., University of Tehran, 2013

A THESIS

submitted in partial fulfillment of the requirements for the degree

MASTER OF SCIENCE

Department of Geology
College of Arts and Sciences

KANSAS STATE UNIVERSITY
Manhattan, Kansas

2019

Approved by:

Major Professor
Dr. Joel Spencer

Copyright

Abstract

In tectonically active arid and semi-arid regions like southern California, alluvial fans and their drainages record not only paleoenvironmental change but also fault movement. To be able to decipher this precious information, a suitable chronological method is required. For events occurring over Late Quaternary timescales, optically stimulated luminescence (OSL) dating is a chronological method that can be used in these settings; however, current OSL approaches are only suited to the fine sand deposits which are present as layers or lenses in the fan architecture. The problem with this sampling approach is that in many fan exposures such deposits are rare, limiting the applicability of OSL. In this study we have investigated the feasibility of a luminescence method for dating fanglomerates by sampling the coarse fraction and extracting the fine sand matrix for dating. Regarding this new approach, issues of partial bleaching and gamma dose-rate heterogeneity should be carefully considered; yet this is worthwhile since this method can greatly expand the applicability of OSL dating in similar settings.

We found that quartz in our sampling area is dim and has poor OSL characteristics, therefore, no ages are calculated based on quartz OSL. On the other hand, K-rich feldspar infrared stimulated luminescence (IRSL) was bright with good characteristics. We also conducted single grain IRSL on three samples (two fanglomerates and a fine sand layer) to investigate the extent of partial bleaching and equivalent dose (De) overdispersion in fanglomerate-derived grains. The data were then modeled with finite mixture model (FMM) using the Luminescence software package in R, allowing us to separate different components in the data. Assessment of gamma dose-rate heterogeneity in the fanglomerate environment was carried out by splitting the fanglomerate samples into <2 mm and >2 mm size fractions, and

comparing data from high-resolution gamma spectrometry and ICP -AES/-MS analyses of the size fractions.

The two fanglomerate sample evaluation demonstrates that single grain analysis and finite mixture modeling (FMM) are essential for De assessment. Fanglomerate dose rate analyses by means of ICP -AES/-MS and high-resolution gamma spectrometry illustrate homogeneous environment for the <2 mm proportions of the samples; however, the >2mm proportions are indicative of dose rate heterogeneity probably due to different lithologies.

Our results from twelve samples indicate that alluvial fan formation in the Coachella Valley happened during both glacial periods and transition from glacial to interglacial periods. In the San Bernardino site, our depositional ages are concordant with the TCN surface age of Owen et al. (2014), indicating fast fan deposition during the marine isotope stage (MIS) 4 (65 ± 10 ka). The paleosol layer (78.81 ± 8.04 ka) beneath this fluvial setting suggest that soil development occurred mainly during the interglacial period MIS 5. In the Indio Hills (north of Biskra Palms) site, almost all depositional ages lie within interglacial periods: MIS 3, MIS 5, MIS 9 and the Holocene.

The calculated minimum slip rate along the Mission Creek fault in Indio Hills area based on the depositional age of sample MC1805 (~75 ka) is 7.0 ± 1.3 to 8.4 ± 1.4 mm/yr. This rate is smaller than the 12.2 to 21.7 mm/yr slip rate along the this fault at Biskra Palms (Behr et al., 2010). Since our OSL age provides a maximum age constraint (i.e. sediment deposition in the alluvial fan prior to offset) and hence a minimum slip rate, this rate could suggest that the slip rate along the Mission Creek fault is constant at least between Biskra Palms and Indio Hills. On the other hand, there is a possibility that the slip rate along the Mission Creek fault has slowed

from the Biskra Palms toward the northwest and the slip might then have been transferred to the Banning fault.

Table of Contents

List of Figures

List of Tables

Acknowledgements

I would like to thank my advisor, Dr. Joel Spencer for his great support and supervision during every step of this project, from field work to analyzing the results.

Thanks to my committee members, Dr. Brice Lacroix, Dr. Lewis Owen, and Dr. Matthew Brueseke for their helpful comments and support.

I would like to thank the KSU Geology Department and specifically the OSL Laboratory, where all sample preparation and multi-grain analysis were carried out.

Special thanks to Dr. Amanda Keen-Zebert for providing the opportunity for single grain measurements at the Desert Research Institute (DRI) OSL Laboratory. I would like to thank Dr. Christina Neudorf for her great help analyzing single grain data and Kathleen Rodrigues for her kind hospitality while I was in Reno.

Great thanks to Dr. Sebastien Huot from the University of Illinois for high-resolution gamma spectrometry analysis.

Thanks to Dr. Paula Marques Figueiredo form the University of Cincinnati for her comments on slip rate analysis.

Thanks to Dr. Arnaud Temme in the Geography Department for his help in landscape and digital elevation model (DEM) analysis.

Thanks to Dr. Rich Koehler from the Nevada Bureau of Mines and Geology at the University of Nevada, Reno for meeting with me and his helpful suggestion on landscape analysis.

Finally, yet as importantly, I would like to thank the financial supporters of this project: the Geological Society of America (GSA); Kansas Geological Foundation (KGF); KSU Geology Department and the OSL Laboratory.

Dedication

To my spouse, Amir Setayesh, who has always encouraged and supported me through all difficulties while being far away from me.

Chapter 1 - Introduction

1.1 - Background

Alluvial fans are important landforms in mountain fronts of arid and semi-arid regions like southern California that record paleoenvironmental changes (e.g. Owen et al., 2014). Southern California has been extensively studied regarding its alluvial fan formation (see section 2.3.1 and references therein), however, the climatic environment most favorable for development of alluvial fans is still debated (Owen et al., 2014). Furthermore, alluvial fans and their drainages can record fault movement in tectonically active areas and if accurate piercing points can be located the amount of offset can be estimated. In combination with the age of the offset feature, the slip rate of the fault can be assessed. Optically stimulated luminescence (OSL) dating is a chronological method that can date sediment deposition directly and can therefore provide valuable information regarding alluvial fan development and past fault movement. Nevertheless, current OSL approaches are only suitable for fine sand deposits that are rare in alluvial fan architecture. In this project, a new OSL approach for alluvial fans is investigated by determining if the course sediment fraction - or fanglomerate - can be dated, enabling potential significant expansion of the applicability of OSL dating in similar settings.

1.2 - Geological Setting and Study Area

Our study area is within the Coachella Valley, southern California. The Coachella Valley is a pull-apart basin related to the transtensive rifting in the Gulf of California (Axen and Fletcher, 1998) which is surrounded by the San Bernardino Mountains to the north, Little San Bernardino Mountains to the east, San Jacinto Mountains to the west, and Salton Sea to the south (e.g. Van Der Woerd et al., 2006; Owen et al., 2014) (Fig 1.1). This region is a tectonically

active semi-arid to arid zone; it has, thus, recorded invaluable evidence of paleoenvironmental conditions, i.e. climatic and tectonic information that has been extensively studied over the late Quaternary period (see table 4 in Owen et al., 2014). The most prominent features that record both climatic change and fault movement in arid and semi-arid areas are alluvial fans and their drainages (e.g. Van Der Woerd et al., 2006; Fattahi et al., 2011; Gray et al., 2014; Owen et al., 2014). Previous studies demonstrate that alluvial fan development and abandonment in the American Southwest seems to be climatically controlled and occurs on a Milankovitch timescale (Spelz et al., 2008; Owen et al., 2014). Owen et al. (2014) show that there are two general periods in which alluvial fan development occurs: the stadial marine isotope stage (MIS) 4 and the Holocene. The slip rate of the Mission Creek fault at Biskra Palms (see Fig. 2.1B) over the last ~50 ka has been estimated at 12.2-21.7 mm/yr (Behr et al., 2010) and 15.9 ± 3.4 mm/yr (Van Der Woerd et al., 2006). The Holocene geologic slip rate for the Banning strand in the northwestern Coachella Valley (Fig. 2.1B) is estimated at ~3.9-4.9 mm/yr (Gold et al., 2015).

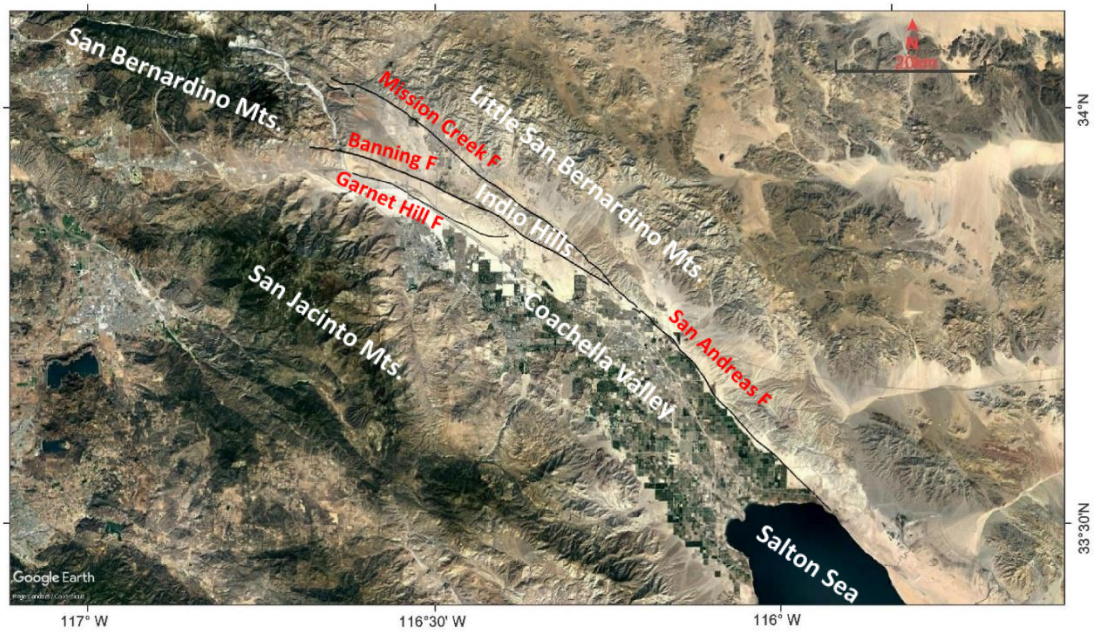

Figure 1.1 Google Earth image of the study area: Coachella Valley is a pull-apart basin surrounded by the San Bernardino Mountains, Little San Bernardino Mountains, San Jacinto Mountains and Salton Sea. Black lines show main fault strands in the valley, adapted from Woerd et al. (2006).

1.3 - OSL Background

Optically stimulated luminescence (OSL) dating is now one of the most reliable chronological methods in dating sediment deposition directly, i.e. to determine the elapsed time since the last exposure of sediments to sunlight (e.g. see review of Huntley and Lian, 1999). This method of dating has been widely used since the first observations of OSL made by Huntley et al. (1985). Since then, extensive work has been done to improve this novel method; among which the single-aliquot regenerative-dose (SAR) protocol has been the most significant development (Murray and Wintle, 2000, 2003; Wallinga et al., 2000; Wintle and Murray, 2006). OSL has been successfully applied during the last decades for ages range from late Pleistocene to Holocene (Rittenour, 2008; Wintle, 2008).

The mineral particularly used in luminescence dating since the late 1990s is quartz (Murray and Olley, 2002), which is one of the most abundant minerals in sedimentary depositss. However, at some localities, this mineral is only present in very small quantities (e.g. Fattahi et al., 2011; Spencer et al., 2012; Fitzgerald et al., 2017) or is not particularly well-behaved (e.g. Lawson et al., 2012; Roder et al., 2012; Rhodes, 2015). Additionally, the quartz luminescence signal becomes saturated with dose and is limited to a maximum age of approximately 100 ka (Buylaert et al., 2012). As a result, other minerals specifically feldspar have been used as dosimeters in luminescence dating (e.g. Fattahi et al., 2011; Thiel et al., 2011; Buylaert et al., 2012; Spencer et al., 2012; Rhodes, 2015; Yi et al., 2016; Fitzgerald et al., 2017).

Nevertheless, using feldspar is not as straightforward as quartz, particularly because of the well-known anomalous fading which affects the original infrared stimulated luminescence (IRSL) measurements of feldspars conducted at 50°C (IR_{50}), leading to age underestimation (e.g. Wintle, 1973; Spooner, 1992, 1994; Huntley and Lian, 1999; Huntley and Lamothe, 2001; Auclair et al., 2003; Lamothe et al., 2003) and the fact that feldspar requires more exposure to sunlight in order to bleach (e.g. Thomsen et al., 2008). However, high-temperature post-infrared infrared-stimulated luminescence (pIRIR) has shown great promise in overcoming anomalous fading (e.g. Thomsen et al., 2008; Buylaert et al., 2009, 2012; Thiel et al., 2011; Sohbati et al., 2012; Yi et al., 2016). In this method the feldspar IRSL is stimulated in a two-step process: the IRSL is measured at 50°C and then this is followed by a second measurement at an elevated temperature (>200°C) (Thomsen et al., 2008). The second high-temperature post-infrared IRSL signal is used for dating analyses.

Utilizing feldspars has further potential advantages:

1) The feldspar IRSL signal saturates at higher radiation dose levels compared to quartz OSL, meaning that it could be suitable for dating older samples (Huntley and Lamothe, 2001; Buylaert et al., 2012; Li et al., 2014);

2) The intensity of IRSL signal is usually much greater than the quartz OSL signal. This means higher precision luminescence measurements (Li et al., 2007) and the ability to date samples when the low intensity of quartz OSL signal impedes dating (e.g. Pye et al., 1995; Lawson et al., 2012);

3) IRSL measurement of feldspar signal means that this mineral can be selectively measured in the presence of other minerals (Huntley and Lamothe, 2001);

4) In sand-sized grains of potassium feldspars, the high internal dose rate from ^{40}K and ^{87}Rb within the crystal lattice reduces the effect of inhomogeneity in the external beta and gamma dose rate and water content on the total dose rate, hence improving precision (Li et al., 2014). However, in this project, the effect of feldspar internal dose rate on the total dose rate may not be as significant since feldspar grains have not been HF-etched and therefore, external alpha dose rate plays an important role as well.

1.4 - This Thesis

In this thesis, we investigated both quartz OSL and feldspar IRSL signals. For feldspar, the $pIRIR_{225}$ protocol was used since it is less prone to anomalous fading compared to IR_{50}. Besides, the $pIRIR_{225}$ luminescence signal is bleached most rapidly compared with other pIRIR protocols (e.g. $pIRIR_{290}$) (Colarossi et al., 2015). However, IR_{50} signals from the $pIRIR_{225}$ sequence were also investigated and compared with $pIRIR_{225}$ results.

We took twelve OSL samples from different alluvial fans that help constrain the timing of alluvial fan formation. These data expand the available alluvial fan chronology and hence climate history of the region. Moreover, the slip rate of the Mission Creek fault, one of the main strands of the San Andreas Fault in the Coachella Valley, is refined.

Our methods, results, discussion and conclusion are presented in Chapter 2 – Manuscript, while Appendices A and B contain all the supplementary data. Chapter 3 represents a comprehensive summary of the discussion and conclusions.

Chapter 2 - Manuscript

Development of luminescence dating methods in tectonically active and arid regions: dating fanglomerates in alluvial fans, Coachella Valley, southern California

Ataee, Nina[1*], Spencer, Joel Q.G.[1], Lacroix, Brice J.[1], Owen, Lewis A.[2]

[1]*Department of Geology, Kansas State University, Manhattan, KS 66506, USA*
[2]*Department of Geology, University of Cincinnati, Cincinnati, OH 45221, USA*
[*]*Corresponding author: ataeen@ksu.edu*

Key words: optically stimulated luminescence, pIRIR, alluvial fan, Mission Creek fault, Coachella Valley

2.1 - Abstract

The Coachella Valley located in southern California is an arid/semi-arid region that hosts active structures, namely the San Andreas Fault. Its climate, in addition to the strike slip system active in this region, allows preservation of paleoclimate and tectonic history in alluvial fans and their drainages. Various chronological methods have been used in these settings to help in our understanding of landscape evolution and tectonic patterns. In this study, we expand the available alluvial fan chronology and refine the slip rate of the Mission Creek fault, one of the main strands of the San Andreas Fault in the Coachella Valley. In addition, a new methodology regarding current OSL approaches is developed by dating the coarse-grained fanglomerates that are abundant in alluvial fans. We will discuss in detail the obstacles such as partial bleaching and gamma dose-rate heterogeneity that will arise regarding this methodology and possible solutions. Our results from twelve samples indicate that alluvial fan formation in the Coachella Valley happened during the glacial period MIS 4 (65 ± 10 ka); interglacial periods MIS 3 (51.04 ± 5.36

ka), MIS 5 (75.83 ± 8.68 ka and 100.24 ± 11.23 ka) and MIS 9 (320.17 ± 33.82 ka); and the Holocene. Slip rate along the Mission Creek fault (7.0 ± 1.3 to 8.4 ± 1.4 mm/yr) seems to have slowed from the Biskra Palms towards northwest, east of San Bernardino Mountains.

2.2 - Introduction

Southern California is one of the best studied regions regarding its tectonic and climatic history. This tectonically active arid to semi-arid zone is a natural laboratory that has recorded invaluable paleoenvironmental information specifically over the late Quaternary period (e.g. Van Der Woerd et al., 2006; Frankel et al., 2007a; Behr et al., 2010; Owen et al., 2014). The most prominent features that record both climatic change and fault movement in arid and semi-arid areas are alluvial fans and their drainages (e.g. Spelz et al., 2008; Owen et al., 2014). However, in order to decipher this precious information a suitable chronological method is required. The well-established radiocarbon dating technique is not usually suitable in this context due to the lack of preserved organic matter in arid and semi-arid environments (Owen et al., 2014). Additionally, the age range for radiocarbon dating is limited to 50 ka. Other methods that have been used in these settings are optically stimulated luminescence (OSL) and thermoluminescence (TL) dating, terrestrial cosmogenic nuclide (TCN) surface exposure dating, U-series dating, and tephrochronology (e.g. Reheis et al., 1996; Robinson et al., 2005; Owen et al., 2006, 2011; Frankel et al., 2007a, 2007b; Spelz et al., 2008; Spencer and Robinson, 2008; Armstrong et al., 2010; Fletcher et al., 2010; Blisniuk et al., 2012; Rittase et al., 2014; Schildgen et al., 2016). OSL, TL and radiocarbon dating usually date the timing of alluvial fan sedimentation, i.e. depositional ages (Owen et al., 2014). U-series provides minimum ages on landform development by defining the ages of carbonate cement formation (Owen et al., 2014). On the

other hand, TCN dating provides timing of abandonment/ incision of alluvial fan surfaces (Owen et al., 2014).

The successful application of quartz OSL dating in southern California has been demonstrated in a number of studies (Gurrola et al., 2014; Lee et al., 2001; Rittase et al., 2014), but other work has indicated problems of partial bleaching and low sensitivity in quartz OSL (Lawson et al., 2012; Rhodes, 2015; Roder et al., 2012). Current OSL approaches are only suited to the fine sand deposits that are present as layers or lenses in the fan architecture. The problem with this sampling approach is that in many instances such deposits are rare (e.g. Spencer and Robinson, 2008).

In this research, we used luminescence dating to develop the available fan chronology in the Coachella Valley and also refine the slip rate of the Mission Creek fault in the Coachella Valley near Indio Hills to the north of Biskra Palms. In addition, we investigate a luminescence method for dating fanglomerates by sampling the coarse fraction and extracting the fine sand matrix for dating. This new methodology can greatly expand the application of luminescence dating is fluvial settings since sand layers are not usually abundant in alluvial fan architectures. Nonetheless, regarding this new technique, issues such as partial bleaching, that could probably be more significant than sand layer fluvial deposits, and dose rate heterogeneity should be considered. To deal with partially-bleached grains, single grain analyses were performed for both quartz and feldspar grains for three of our samples, including the two fanglomerates. To examine the possible presence of dose-rate heterogeneity, dose rate was measured utilizing ICP -AES/-MS and high-resolution gamma spectrometry and ICP -AES/-MS for >2 mm and <2 mm proportions of the fanglomerate samples.

In the following sections, we will describe the study area (section 2.3) and sampling sites (section 2.4), represent our methods and results (section 2.5), discuss and outline the main findings of the research in discussion (section 2.6) and conclusions (section 2.7).

2.3 - Study Area

2.3.1 - Paleoclimate and Alluvial Fan Formation

Alluvial fans are cone-shaped depositional structures that are formed along mountain fronts where streams leave their confined valleys into a lower gradient piedmont (Bierman and Montgomery, 2014). These features are formed in both arid and humid regions; however, they are more noticeable and better preserved in arid, semi-arid environments. Fan morphologies reflect depositional processes, and hence are changed if the environment and as a result depositional processes are altered (Harvey et al., 1999). Fan depositional or sediment transport processes can be divided into two general categories, fluvial vs. debris flow (Bierman and Montgomery, 2014). Sediments delivered by fluvial transport are better sorted than debris flow deposits and tend to be clast supported, while debris flow deposits are unsorted and matrix supported (diamicts) (Bierman and Montgomery, 2014). Sediment supply and transportation power are important factors controlling the depositional or erosional response of a fan (Bull, 1991; Harvey et al., 1999). These factors can be changed due to tectonic activity, climatic change or intrinsic geomorphic conditions of the fans (e.g. Harvey et al., 1999).

As mentioned, alluvial fans are one of the most common landforms in mountain front areas in arid and semi-arid regions (e.g. Reheis et al., 1996; Owen et al., 2014) that are highly sensitive to environmental changes and therefore, exceptional archives of climate and tectonic records (e.g. Lecce, 1990; Ritter et al., 1995; Reheis et al., 1996; Harvey et al., 1999; Owen et

al., 1997, 2006; McDonald et al., 2003; Quigley et al., 2007; Frankel et al., 2007a, 2007b; Spelz et al., 2008; Miller et al., 2010; Owen et al., 2014). Alluvial fan formation and development can be caused by tectonic activity, climatic change or intrinsic geomorphic conditions (Harvey et al., 1999). Numerous researchers have studied alluvial fan formation in the American southwest (e.g. Sharp et al., 1959; Ponti, 1985; Wells et al., 1987; Reheis et al., 1996; Harvey et al., 1999; McDonald et al., 2003; Owen et al., 2003; Frankel et al., 2007a, 2007b; Spelz et al., 2008; Armstrong et al., 2010; Blisniuk et al., 2010; Fletcher et al., 2010; Miller et al., 2010; Owen et al., 2011; Blisniuk et al., 2012; Owen et al., 2014). Although alluvial fan formation is believed to be climatically controlled, the exact climatic transition that results in fan development in desert environments like southern California is still debated. There are two models explaining the alluvial fan formation in desert environments: the first one is associated with transition from humid to arid conditions or a relative increase in aridity (e.g. Bull, 1977, 1991, 2000; Wells et al., 1987), and the second is associated with the transition from arid to humid conditions or a relative increase in rainfall (e.g. Ponti, 1985; Harvey et al., 1999). Alluvial fan formation in the American southwest is generally believed to be in accordance with the arid model stating that aggradation of alluvial fans overlaps with transitions from glacial to interglacial cycles (Owen et al., 2014). However, to test this widely accepted model, Owen et al. (2014) compiled all existing data on alluvial fan formation in the American southwest (their Table 4 and Fig. 11) showing that the pattern of alluvial fan formation in this region is complex with a strong climatic control. Alluvial fan ages in the American southwest cluster at numerous times through the Late Quaternary and it seems that fan development and abandonment occurs on a Milankovitch timescale (Fig 10, Spelz et al., 2008; Fig. 12, Owen et al., 2014). However, there are two general periods in which alluvial fan development occurs: the stadial marine isotope stage (MIS) 4 and

the Holocene; suggesting that the arid alluvial fan model might not be valid (Owen et al., 2014). Alluvial fans also formed during late MIS 3 and MIS 2 in areas such as Baja California, Southern Transverse Ranges and Owens Valley; nevertheless, some of these regions have been influenced by glaciers and hence the alluvial fans are paraglacial (Owen et al., 2014).

2.3.2 - Tectonics

Recent moderate to large earthquakes, such as the ML 5.9, 1986 North Palm Springs (Jones et al., 1986) as well as several events recognized via paleoseismology since 800 A.D. have occurred in the Coachella Valley (Rockwell et al., 2016). Coachella Valley is a pull-apart basin related to the rifting in the Gulf of California (Fig 2.1A) (Gray et al., 2014). The San Andreas Fault (SAF) in this area is composed of low-relief strike-slip segments bounded by high-relief transpressive segments (Spotila et al., 2007) and splays into three strands (Mission Creek, Banning, and Garnet Hill) that merge towards the southeast into a single strand near Biskra Palms (Fig. 2.1B) (Heermance and Yule, 2017). The transpressive segments in this area are the Indio, Mecca, and Durmid Hills that demonstrate considerable deformation and uplift (Sylvester and Smith, 1976; Gray et al., 2014).

To the north of the Coachella Valley, the eastern end of the San Bernardino Mountains rises from the Salton Sea at 69 m below sea level in the Salton Trough to the top of San Gorgonio Mountain at 3506 m above sea level, in less than 100 km (Fig. 1.1) (Owen et al., 2014). There is a large bend in the SAF causing transpressional uplift in this area (Blythe et al., 2000; Owen et al., 2014). The Mission Creek is a right lateral strike-slip fault and the Banning is an oblique strike-slip thrust fault, which converge at the eastern end of the Indio Hills to form a single strand of the SAF (Fig. 2.1B) (Owen et al., 2014). Tectonics and strain partitioning

between active strands of the SAF system has a significant role in forming the geomorphology of this area. As a result of this partitioning, understanding how the strain can be transferred is fundamental; therefore, estimating the slip rate for different strands is a key factor (Van Der Woerd et al., 2006; McGill et al., 2013, 2015). The slip rate of the Mission Creek fault at Biskra Palms over ~50 ka is estimated at 12-22 mm/yr (Behr et al., 2010); or 15.9 ± 3.4 mm/yr (Van Der Woerd et al., 2006). The Holocene geologic slip rate for the Banning strand is estimated at ~3.9-4.9 mm/yr which represents only 25–35% of the total slip by this section of the southern San Andreas Fault (Gold et al., 2015). However, Gold et al. (2015) suggest the onset of more significant slip transfer from the Mission Creek to the Banning strand to the northwest of Thousand Palms Canyon in Indio Hills area, over both long-term (Quaternary) and short-term (Holocene) timescales, based on the abrupt increase in topography, relief, stream incision, erosion and structural evidence.

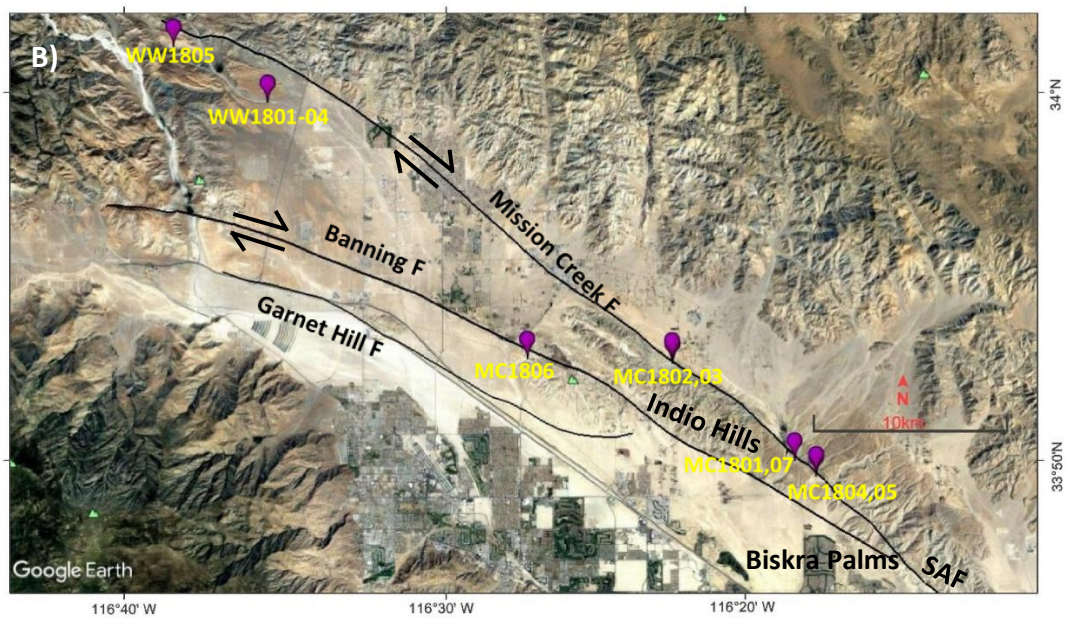

Figure 2.1 Google Earth images of the study area: A) Coachella Valley is a pull-apart basin related to transtensive rifting in the Gulf of California. Red box shows the study area. B) Study area indicating six sampling sites. Three main strands of the San Andreas Fault pass through the Coachella Valley: Mission Creek Fault, Banning Fault and Garnet Hill Fault. Fault lines adapted from Woerd et al. (2006).

2.4 - Sampling Sites

We have six main sampling locations in the Coachella Valley and collected twelve samples (Fig 2.1B); at two of these locations we collected fanglomerate samples in black plastic bags at night. Five samples (WW1801-05) were collected in the northwest of the Coachella Valley in the eastern San Bernardino Mountains, six samples (MC1801-05 and MC1807) were collected along the Mission Creek fault north of Biskra Palms, and one sample (MC1806) was collected from an exposure along the Banning fault.

To test the accuracy of the fanglomerate dating approach, we have devised the following sampling methodology: collected samples in stratigraphic superposition; targeted fine sand

lenses where available; and one of our fanglomerate sampling sites correlates with existing TCN chronology.

2.4.1 - Mission Creek_ Eastern San Bernardino Mountains

The site with existing TCN chronology is located at the eastern end of the San Bernardino Mountains (alluvial fan Fm4b in Owen et al., 2014). The surface of Fm4 rises about 15-25 m above the present stream level and one of its best exposures is present in alluvial fan surface Fm4b on the southern side of Mission Creek (Fig 2.2A) (Fig 4B, Owen et al., 2014). We collected four samples from this alluvial fan exposure: WW1801 and WW1802 were sampled in a sand layer (low-angled cross-stratified channel fill sands, sedimentary unit C, Fig. 4B, Owen et al., 2014) and are separated horizontally by ~2 m (Fig 2.2B); WW1803 was collected from the adjacent fanglomerate layer (pebbly diamicts, sedimentary unit E, Fig. 4B, Owen et al., 2014) (Fig 2.2B); WW1804 was collected in a paleosol layer (Fig. 4B, Owen et al., 2014) ~30 m west and ~1.5 m below these samples (Fig 2.2C). Sample WW1805 (fine sand, with a few 1 to 2 cm-sized pebbles) was collected from an exposure of an alluvial fan called Fm1b in Owen et al. (2014) (Fig 2.3). Table 2.1 shows the location, altitude and depth of each sample.

Based on Owen et al. (2014) the Mission Creek alluvial fan complex consists of six morphostratigraphically discrete gently sloping surfaces, that traverse the Mission Creek fault and trend ESE into the Coachella Valley (Fig 2.4); and consist of bouldery debris deposits that demonstrate deposition dominated by high magnitude-low frequency large debris flows and flash floods, with sporadic stream flows (Fig 2.2).

2.4.2 - Mission Creek_ North of Biskra Palms

We have three main sampling sites along the Mission Creek fault to the north of Biskra Palms (Samples MC1801-05 and MC1807) (Fig. 2.1). Sample MC1801 was collected from a sand dominated layer (fine sand, with a few 2 cm-sized pebbles) in natural exposure of an alluvial fan along the Mission Creek fault (Fig 2.5), and fanglomerate sample MC1807 which is a cobbly matrix supported sedimentary unit was collected ~20 m to the east of MC1801. Sample MC1805 (fine sand, with occasional ~2 cm pebbles) was taken in an alluvial fan exposure where the main drainage was displaced by the Mission Creek fault (Fig 2.7A) and sample MC1804 (fine sand, with occasional pebbles ~0.5-1 cm) was taken in a young channel nearby (Fig 2.6) (see Table 2.1 for exact locations). Sample MC1802 was collected in an alluvial fan which is apparently an older feature compared to the rest of the fans based on its very consolidated texture. Sample MC1803 (fine sand layer, mainly <1 mm) from a nearby exposure (Fig 2.6). Sample MC1806 (matrix-supported sand layer with a few 1 to 2 cm pebbles) is the only sample that was collected in an exposure along the Banning fault (Fig 2.7B).

A)

Fm4b

^{10}Be TCN

63.0 ± 2.6 ka

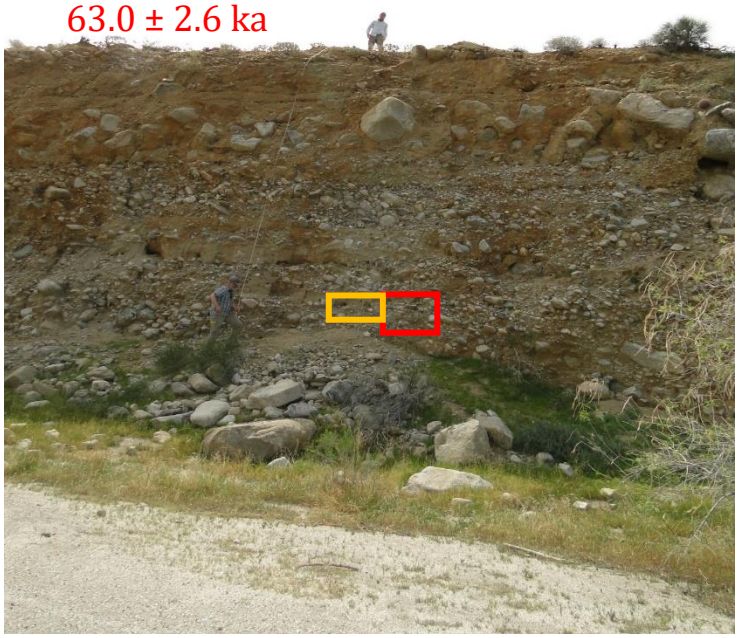

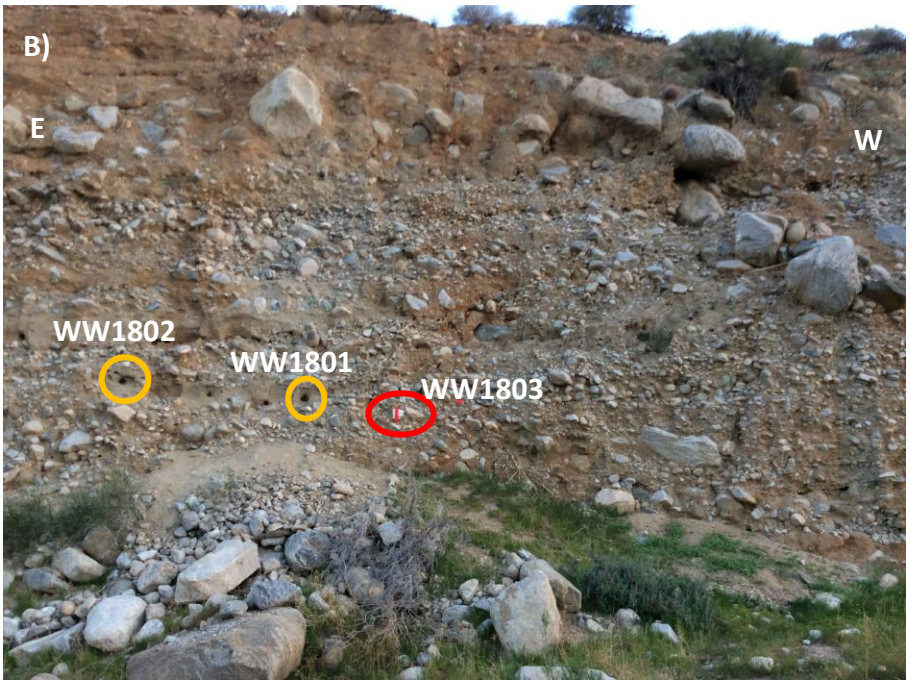

Figure 2.2 A) Alluvial fan Fm4b where samples WW1801 to 04 were collected. Yellow box shows the location of sand lens where samples WW1801 and 02 were collected. Red box indicates the adjacent fanglomerate layer where WW1803 sample was collected. Name of the fan and ^{10}Be TCN surface age adapted from Owen et al. (2014). Bouldery debris deposits show deposition dominated by flash floods. B) Close-up of the exposure. Samples WW1801 and 02 were collected in the sand lens and are ~2 m apart horizontally. WW1803 collected within the fanglomerate layer located exactly next to the sand lens. C) WW1804 is collected in the paleosol layer ~30 m west and ~1.5 m below these samples.

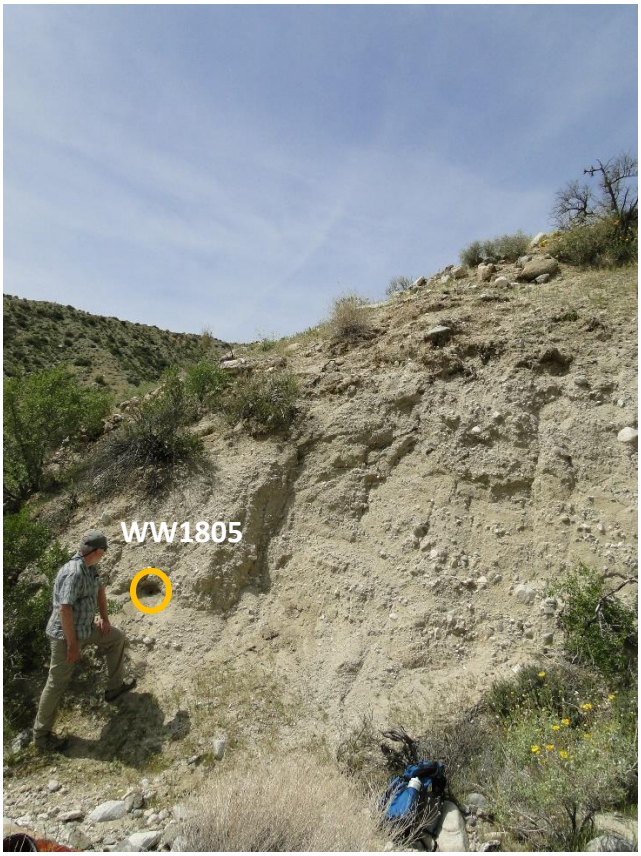

Figure 2.3 Sample WW1805 taken from a natural exposure of the alluvial fan Fm1b in the Mission Creek alluvial fan complex (based on Owen et al., 2104).

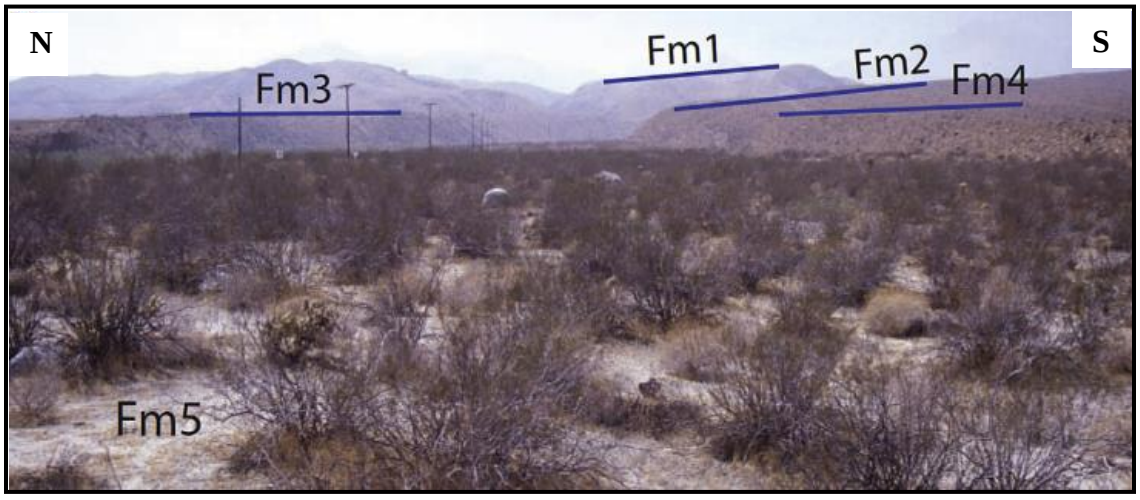

Figure 2.4 Mission Creek alluvial fan complex showing alluvial fan surfaces Fm1 through Fm5. Modified from Owen et al. (2014).

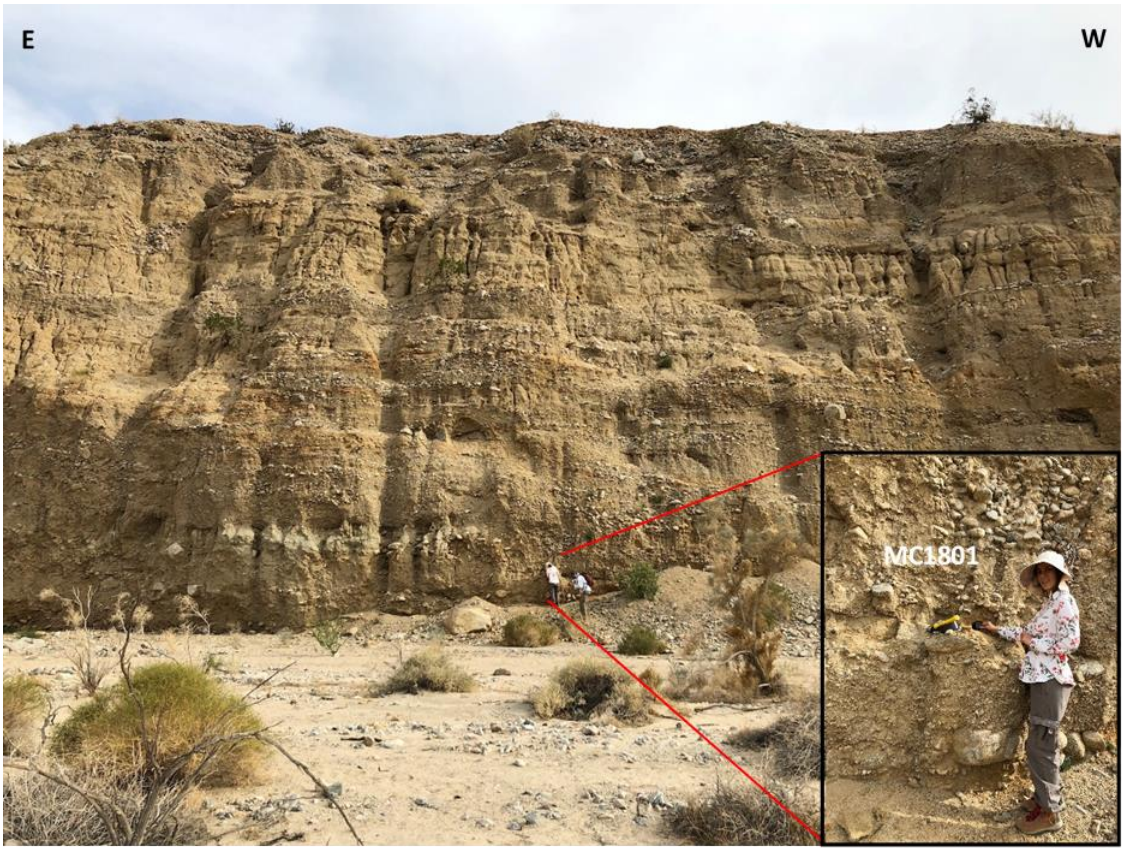

Figure 2.5 Sample MC1801 collected at a natural fan exposure along the Mission Creek fault. Sample MC1807 collected at night from a fanglomerate layer ~20m to the east.

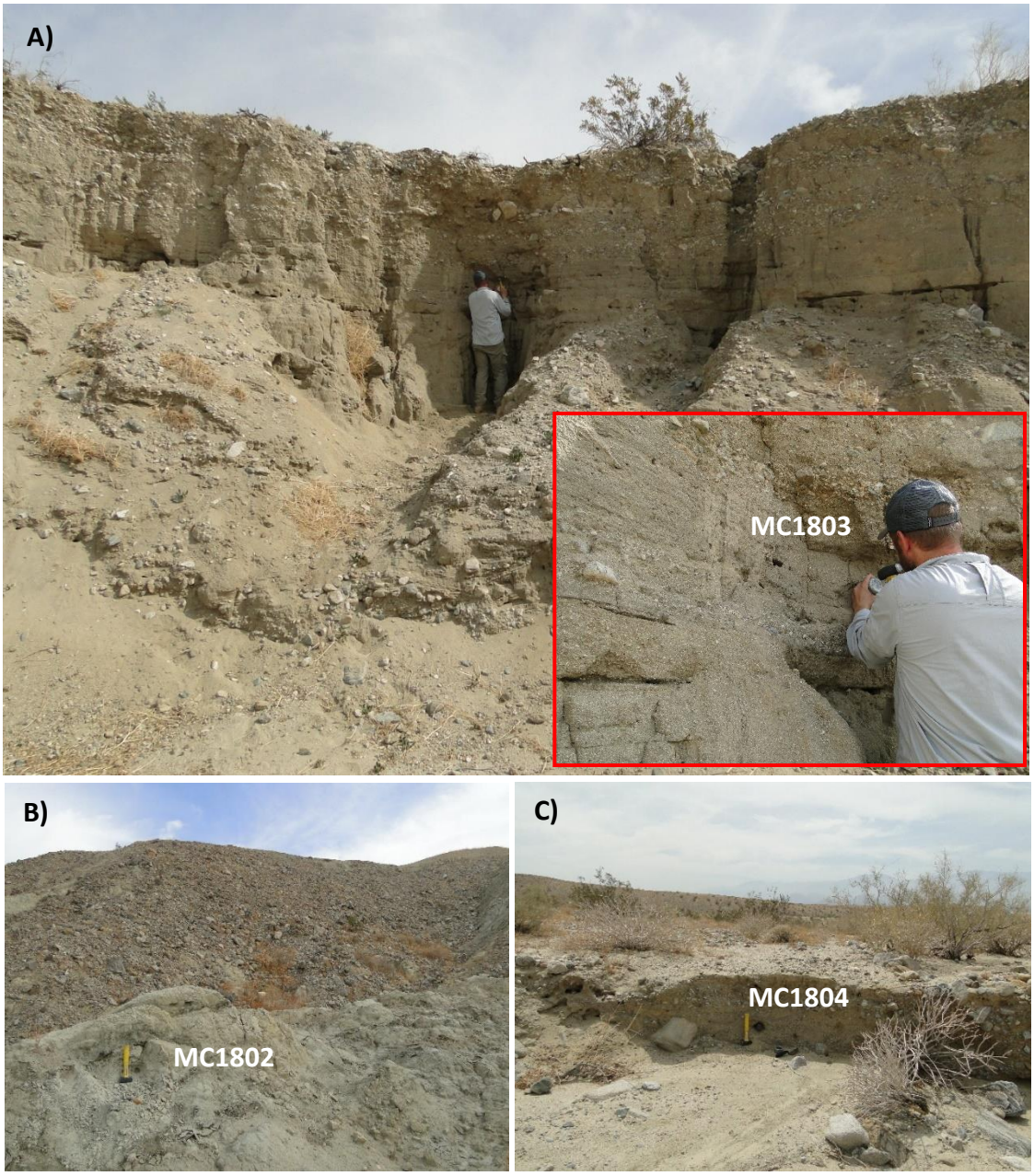

Figure 2.6 A) Sample MC1803, B) sample MC1802 taken from a supposedly older alluvial fan (see the argument in section 2.4.2), C) sample MC1804 gathered from a recent channel.

Figure 2.7 A) Sample MC1805, B) sample MC1806 taken from a road-cut.

Table 2.1 Sample location, altitude and depth.

Sample	Latitude °N	Longitude °W	Altitude (m)	Depth (m)
WW1801	33.9963	116.5978	573	11.1
WW1802	33.9963	116.5978	573	11.1
WW1803	33.9963	116.5978	573	11.1
WW1804	33.9963	116.5978	573	12.6
WW1805	34.0211	116.6488	831	2
MC1801	33.8332	116.3067	147	20
MC1802	33.8775	116.3745	284	0.5
MC1803	33.8793	116.3747	263	2
MC1804	33.8257	116.2948	121	0.5
MC1805	33.8269	116.2948	177	1.5
MC1806	33.8799	116.4546	259	1
MC1807	33.8332	116.3067	147	20

2.5 - Methods and Results

2.5.1 - Digital Elevation Model (DEM)

Strike slip fault systems like the San Andreas Fault cause offset in alluvial fans and channels as they creep or generate earthquakes (e.g. Van Der Woerd et al., 2006; Frankel et al., 2007a; Behr et al., 2010; Gold et al., 2015). This offset can be preserved in arid, semi-arid regions like southern California as the weathering and erosion processes are slowed down by the lack of humidity and chemical weathering. As a result, these areas can be considered natural laboratories preserving the evidence of faulting and hence, making it possible to measure slip rate over different time scales (based on the age of the offset feature) (e.g. Van Der Woerd et al., 2006; Frankel et al., 2007a, 2007b; Behr et al., 2010; Gold et al., 2015). However, we need piercing points to be able to accurately reconstruct the offset channels or beheaded alluvial fans

and it is not always straightforward to find the exact location of these piercing points. Fan surface morphology is commonly used to distinguish alluvial fans of different ages (e.g. Wells et al., 1987; Bull, 1991; Ritter et al., 1993). It is possible to observe different surface roughness morphologies on aerial photos based on depth of channel incision and color contrast of the fan surface. Based on Google Earth imagery we can observe a series of raised beheaded alluvial fans, shutter ridges and displaced channels in the study area. Three beheaded alluvial fans along the Mission Creek fault trace were identified (Fig 2.12). It is not possible to match Fans 1 and 2 with any feature to the northeast side of the fault. Part of Fan 3 is preserved, yet, it is challenging to find a piercing point. To investigate this in more detail a 1 m digital elevation model (DEM) from lidar data available from the B4 project on the OpenTopography website (http://opentopo.sdsc.edu/datasets) was utilized. This high-resolution DEM is only available along major fault traces in California. Fig 2.13 shows the calculated hill-shade using ArcGIS based on B4 DEMs. Based on the hill-shade, displacement of fan 3 is more evident. To locate piercing points, we investigated surface roughness map as well. Surface roughness is defined as the standard deviation of slope and will average out surface features (eliminating any anomalies), hence, making it easier to perceive different depth of incision for different drainage generations (Frankel and Dolan, 2007). This map was generated applying the Focal Statistics tool in the ArcGIS program (Fig 2.14A). To reconstruct the displacement of Fan 3, three scenarios can be considered based on the roughness map; with displacements 530 m, 570 m and 640 m (Fig 2.14A shows the three piercing points and Fig 2.14B shows reconstruction of one of the scenarios). It is not possible to reconstruct the displacement of the channel itself due to erosion-deposition on channel edges.

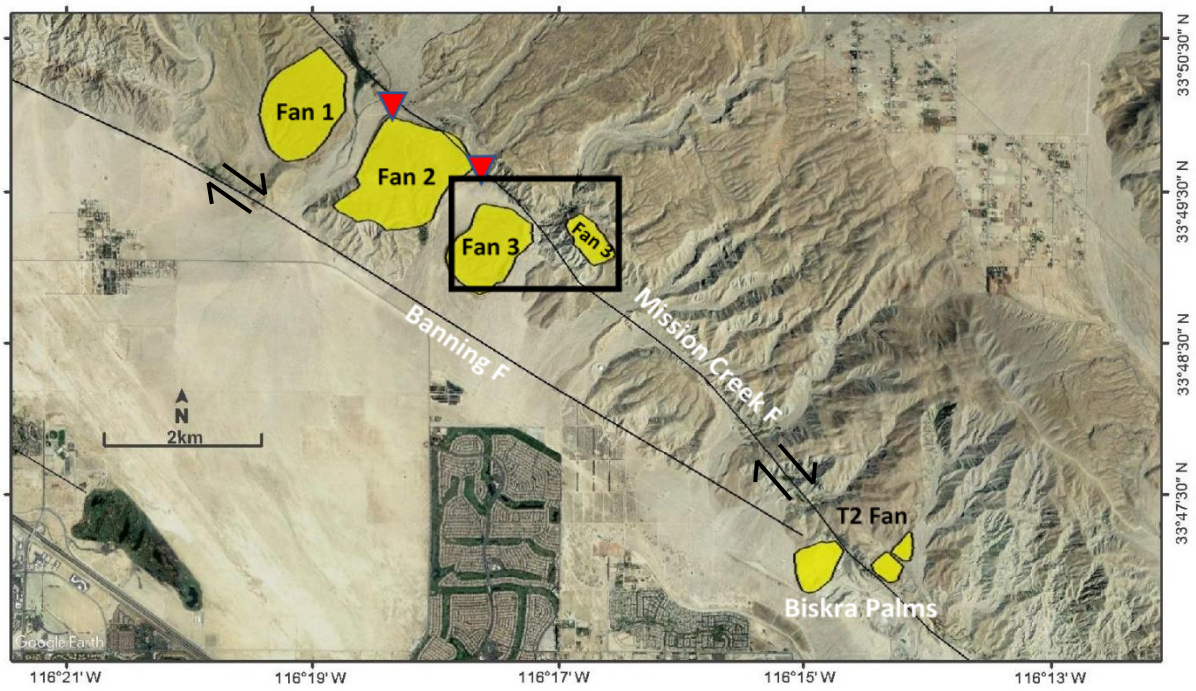

Figure 2.8 A series of alluvial fans along the Mission Creek fault north of Biskra Palms. The name T2 fan is adopted from Woerd et al. (2006). Fans 1, 2 and 3 are beheaded alluvial fans and mapped based on surface morphology (color, elevation and depth of incision), however, piercing points were only measured on Fan 3. Inset box indicates the area shown in Figs 2.13 and 2.14 Red triangles show sampling locations.

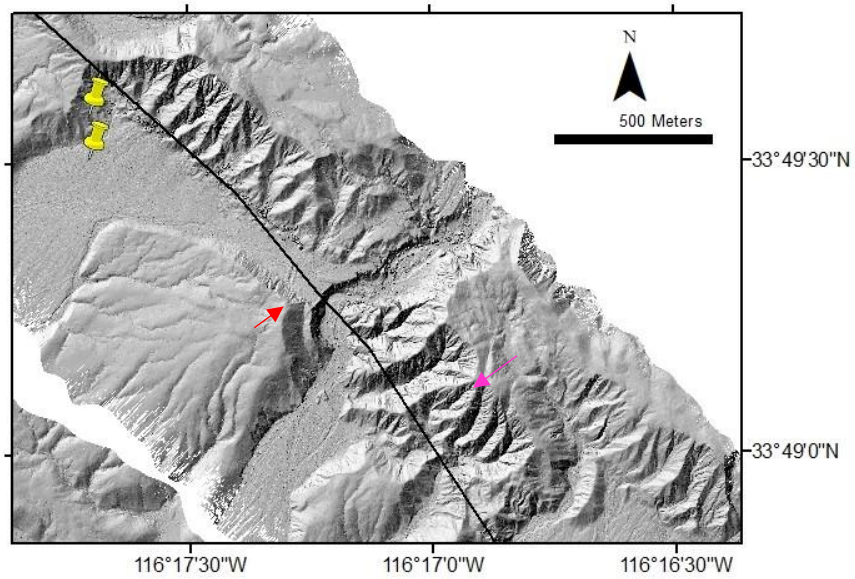

Figure 2.9 Hill-shade of beheaded Fan 3 generated on 1m Lidar DEMs from the B4 project accessible at OpenTopography website. Yellow pins show sampling locations (MC1804, 05).

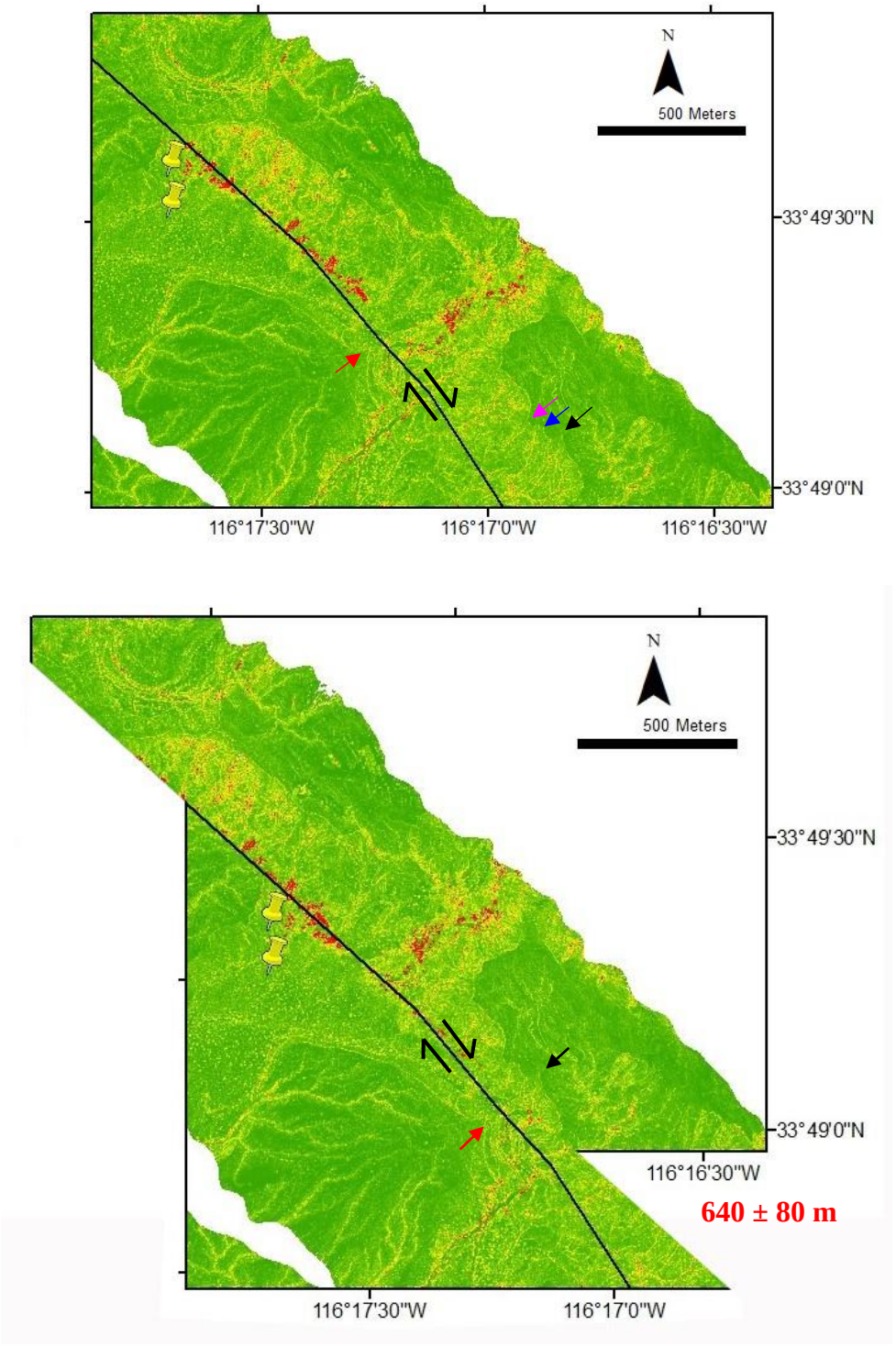

Figure 2.10 A) Surface roughness map of beheaded Fan 3 generated on 1m Lidar DEMs from the B4 project accessible at OpenTopography website. Red arrow indicates the matched mid-point on the SW side of Fan 3. The pink, blue and black arrows show three different offset scenarios: 530 m, 570 m and 640 m, respectively. B) Reconstruction of Fan 3 for the black arrow in Fig 2.14A. Yellow pins show sampling locations (MC1804, 05).

2.5.2 - Sample collection and preparation

Samples from sand layers were collected using steel tubes (length: 14 cm, diameter: 4 cm) hammered horizontally into the sediment exposures. Care was taken to minimize daylight exposure. The section was first cleaned back to remove weathered and loose sediment and reveal primary bedding structures. It is also critical to ensure that tubes are completely full to prevent mixing of the light-exposed grains at the end of the tubes with the sediment in the middle.

The two fanglomerate samples (WW1803 and MC1807) were collected in light-proof black plastic bags at night using headlamps with low-intensity red LEDs. We used a cold chisel and 2 lb hammer. Firstly, the outer layer of fanglomerate material was cleaned back a few centimeters to remove weathered and loose sediment, then with light taps on the cold chisel we gently loosened portions of fanglomerate and allowed these to fall into light-proof plastic bags held below the sampled deposit. We also collected duplicate fanglomerate samples during daylight for dosimetry and tagged sampling sites so that they could be found again in the dark.

Samples were analyzed at the Luminescence Research and Dating Laboratory, Kansas State University. Preparation of samples from sand layers followed standard procedures (Spencer et al., 2012, 2015); initial preparation steps for fanglomerate samples were modified. All samples were prepared under very low intensity amber lighting (Spencer et al., 2012). To minimize the likelihood of including any light-exposed grains with grains in the interior of the tube, ~2-3 cm at each end of the tube samples were carefully separated and used for environmental dose rate analysis (see section 2.5.6). Then all samples were dried in a 50°C oven to record field moisture. In order to separate grain-size fractions, 100 g of the sediment was dry-sieved using mesh sizes of 90, 125, 170, 212, 250, and 300 μm. For the fanglomerate samples, firstly the sand matrix was separated from the coarser clasts using a metal sieve with a 2 mm mesh size. Then the finer sand

was separated using a second sieve (500 µm metal mesh). The remaining <500 µm sand was dry-sieved following the same steps mentioned above. Grain size distribution of a fanglomerate sample was compared to a tube sand-layer sample in Figs 2.8 and 2.9. Further preparation steps described below were the same for the sediment from tube samples and fanglomerate samples.

Selected grain size for each sample is the modal size for fractions <250 µm; which was 125-170 µm for all samples except for MC1802 (90-125 µm). The selected grain size was treated with 10% hydrochloric acid (HCl) for ~30 min to remove carbonates followed immediately by 30% hydrogen peroxide (H_2O_2) wash for ~3 days to remove organic matter. To isolate quartz and potassium-rich feldspar (K-feldspar) from heavy minerals a two-step floatation in lithium metatungstate (LMT) solutions of 2.70 g/cm^3 and 2.58 g/cm^3 was employed (Aitken, 1985). Following density separation, K-feldspar (<2.58 g/cm^3) grains were not etched using hydrofluoric acid (HF) due to concerns regarding the anisotropic removal of the surface (Colarossi et al., 2015; Duval et al., 2015). The density fraction that isolates quartz grains (2.58-2.70 g/cm^3) was etched for ~40 min in 48% HF which dissolves feldspars (particularly plagioclase and sodium-rich feldspars), and removes an ~10-20 µm rind from quartz minimizing luminescence due to alpha particle radiation external to the grain. HF treatments were followed by ~30 min 10% HCl treatment to remove any precipitated fluorides and then the grains were re-sieved.

All multi-grain aliquots were made using a 1 or 3 mm spray mask and then spraying silicone oil onto stainless steel discs (1 cm diameter) followed by spreading a layer of grains on the center of the disc (where oil is positioned). Total number of 125-170 µm grains on a 1 mm aliquot is approximately 35 to 64 grains which will increase to ~64 to 124 grains for grain size 90-125 µm. The quartz OSL and feldspar IRSL results are discussed below.

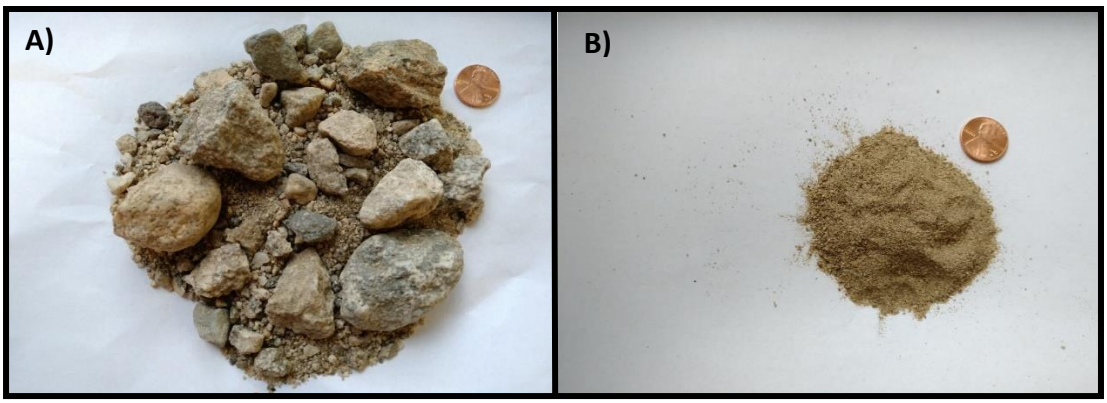

Figure 2.11 Photos of A) a fanglomerate sample (WW1803), and B) a sand-layer sample (WW1801). Penny for scale.

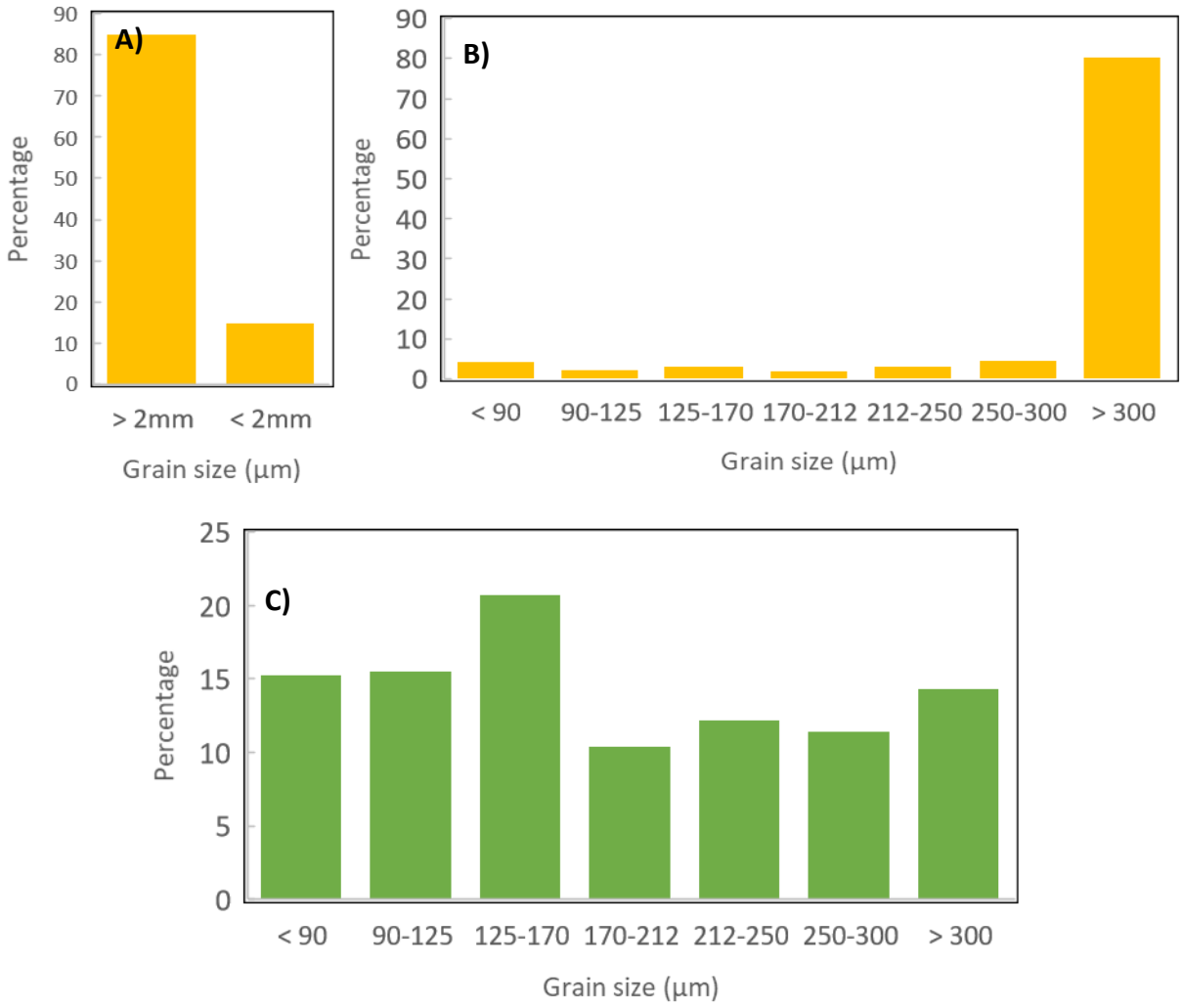

Figure 2.12 A) and B) Grain size distribution of a fanglomerate layer sample (WW1803). Before the common sieving process, sand matrix was separated from coarse clasts with a 2 mm sieve. C) A sand-layer grain size distribution (WW1801).

2.5.3 - OSL Measurements of Quartz

All multi-grain luminescence measurements were made using a standard Risø TL/OSL reader model DA-20 equipped with a $^{90}Sr/^{90}Y$ beta source with a dose rate ~0.13 Gy/s. Blue LEDs (470 nm) were used for quartz stimulation and signals were collected through 7.5 mm of Hoya U-340 (UV) filter (Bøtter-Jensen et al., 2003). Aliquots were made on 10 mm stainless steel discs. Standard single-aliquot regenerative-dose (SAR) protocol was employed (Murray and Wintle, 2000). We started our investigations with 1 mm diameter multi-grain aliquots of quartz; almost all aliquots were dim (Fig 2.10A) with poor OSL characteristics (recycling and recuperation ratios). Consequently, we increased the aliquot size to 3 mm, however, the OSL signal for most aliquots was still poor (dim with weak or absent fast component) (Fig 2.10B). Quartz OSL signals were investigated for all samples, demonstrating generally dim signals with poor OSL characteristics. Therefore, no equivalent dose (De) was calculated based on quartz OSL.

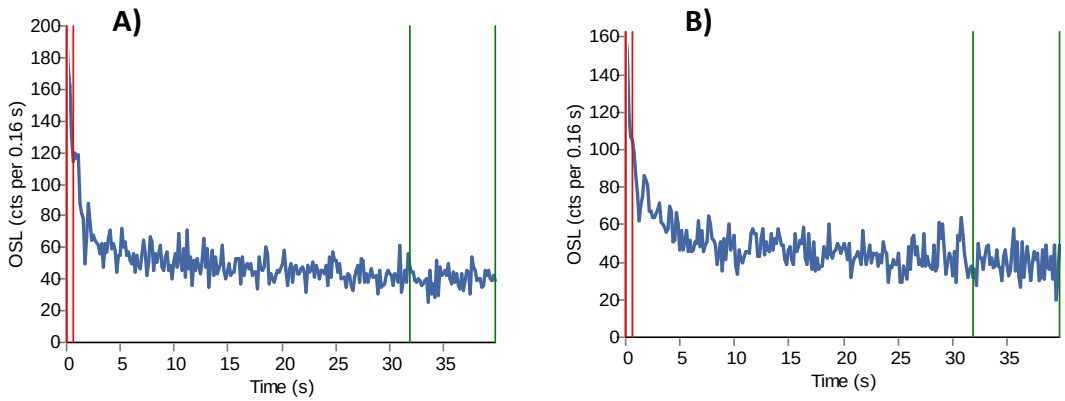

Figure 2.13 Example of quartz natural OSL signal for A) 1 mm aliquot of sample MC1801, and B) a 3 mm aliquot for sample WW1801. Signals are very dim with weak or absent fast component.

2.5.4 - IRSL Measurements of Feldspar

For feldspar, infra-red LEDs (870 nm) were used for stimulation and signals were detected in the near-UV to blue spectral range through a combination of 2 mm Schott BG-39 and 4 mm Corning 7-59 filters with an EMI 9235QB photomultiplier tube (PMT) (Spencer et al., 2012). Multi-grain aliquots 1 mm-in-diameter were dispensed onto 10 mm stainless steel discs. A SAR protocol for post-infrared IRSL (hereafter referred to as pIRIR) modified from Roozeboom (2015) (Table 2.2) was used to determine De values; preheat and measurement temperature was adopted from Thomsen et al. (2008, 2011). The $pIRIR_{225}$ protocol as outlined in Table 2.2 is composed of 9 steps. Step 1: administering the natural or a regenerative dose; step 2: 250°C preheat for 60 s; step 3: IR stimulation for 100 s at 50°C sample temperature (IR_{50}); step 4: second IR stimulation for 100 s at 225°C sample temperature ($pIRIR_{225}$); steps 5 through 8: repeat of the same measurements from steps 1 through 4, except that in step 5 a constant test dose is administered in each cycle; step 9: hot-bleach (IR stimulation at 290°C sample temperature). Tx data from steps 5 through 8 is used to correct for any luminescence sensitivity change in each cycle of the SAR protocol. The purpose of the preheat is to remove unstable charge from electron traps before the measurement of the luminescence signal. The hot-bleach is specifically used in feldspar IRSL measurements to remove any remaining charge in electron traps before the following cycle. The size of the test dose for each sample was decided based on the De for that sample and for most of our samples is between 5 to 15% of the average De. The initial 2 second integral and final 20 second integral of the decay curve were selected for IRSL and background signal, respectively (Fig 2.11A). Fig 2.11B demonstrates a SAR growth curve where the x-axis is the regenerative dose, and the y-axis represents the sensitivity-corrected IRSL signal.

In this study, we selected the $pIRIR_{225}$ since this protocol is less prone to anomalous fading compared with IR_{50}, however, fading rates has been measured. Furthermore, $pIRIR_{225}$ is more effectively bleached than $pIRIR_{290}$ (Colarossi et al., 2015; Roozeboom, 2015) which is crucial for this study because alluvial fan depositional processes generally have poor bleaching efficiency that will become more significant in fanglomerate deposition compared to sand layers. Moreover, the $pIRIR_{225}$ results are compared with the IR_{50} results measured within the same sequence. The multi grain results were modeled with the central age model (CAM) and minimum age model (MAM) (Galbraith et al., 1999) utilizing the luminescence software package (Burow, 2018) in R (see section 2.5.11). Multi grain kernel density estimate (KDE) diagrams and radial plots are presented in Appendix A.

Table 2.2 Post-IR IRSL ($pIRIR_{225}$) SAR sequence based on Thomsen et al. (2008, 2011). Equivalent doses (De) were calculated for IR_{50} (steps 3 and 7) and $pIRIR_{225}$ (steps 4 and 8).

Step	Treatment	Observed
1	Regenerative Dose	
2	Preheat: 60 s at 250 °C	
3	IR stimulation: 100 s at 50 °C	Lx
4	IR stimulation: 100 s at 225 °C	Lx
5	Test dose	
6	Preheat: 60 s at 250 °C	
7	IR stimulation: 100 s at 50 °C	Tx
8	IR stimulation: 100 s at 225 °C	Tx
9	IR stimulation: 100 s at 290 °C	
10	Return to step 1	

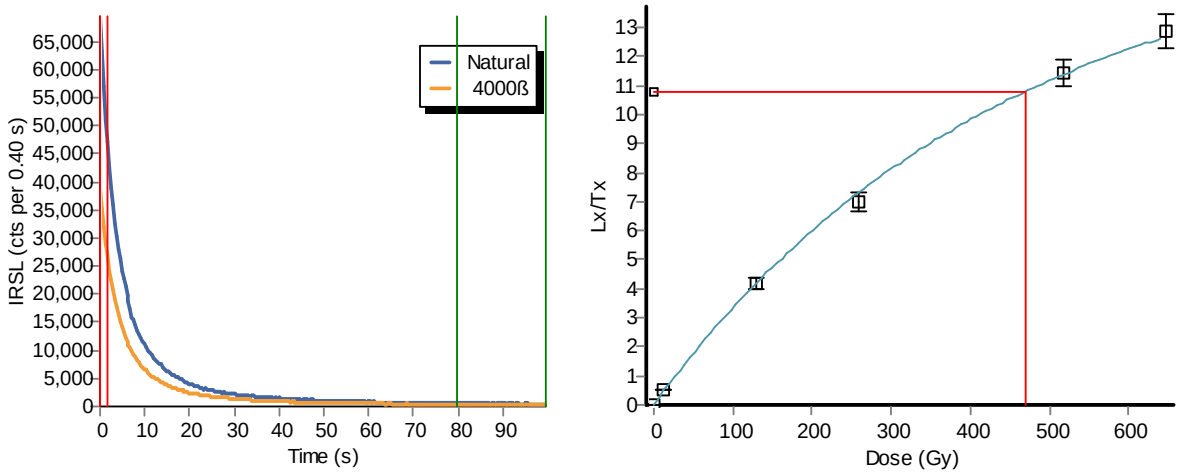

Figure 2.14 A) pIRIR$_{225}$ decay curve of feldspar for sample WW1803, the initial 2 second integral and final 20 second integral of the decay curve were selected for IRSL and background signal, respectively. B) Its corresponding growth curve. Recycling ratio: 0.98 ± 0.06, Recuperation ratio: 0.2 ± 0.0 %. The natural pIRIR$_{225}$ is plotted on the Y axis and then interpolated to X axis through the growth curve (De: 468.82 ± 18.99 Gy).

2.5.5 - Single Grain Measurements

All single grain luminescence measurements were made using two standard Risø TL/OSL readers model DA-20 equipped with green and IR laser single-grain dating attachments and ^{90}Sr/^{90}Y beta source with dose rates ~0.13 Gy/s and ~0.11 Gy/s at Desert Research Institute luminescence laboratory (DRILL), Reno.

The two fanglomerate samples (WW1803 and MC1807) and one sand layer sample (WW1801) were analyzed by means of single grain measurements. The main reason for single grain analysis is exclusion of outliers (e.g. poorly bleached grains) that may lead to a bias in age estimates especially for relatively high-energy fluvial contexts (Rhodes, 2015b). Performing single grain analysis increases the ability to measure grains that have been completely bleached, and therefore more readily statistically discriminate bleached from unbleached grains. This way better estimates of the true burial dose for more complex deposits such as fanglomerates can be obtained. The two fanglomerate samples (WW1803 and MC1807) were analyzed using single

grain measurements since the possibility of having outliers is higher in our fanglomerate samples. Their heterogeneous environment that contains relatively large clasts (as big as ~5 cm in diameter) indicates the depositional process to be more energetic, rapid, and turbid than a sand deposit. As a result, a higher proportion of grains which are partially bleached or unbleached is expected. The analysis of sample WW1801 allowed comparison of a sand layer with fanglomerate results (see Fig 2.2B for relative location of WW1801 and WW1803).

For single grain analysis 212-250 μm grain size was used. This is because the holes in single grain discs fit this grain size, so if using smaller grain sizes then more than one grain can fit in a hole which is not favorable for single grain measurement. First, quartz OSL signals were inspected using a 10 mW Nd:YVO_4 solid state diode-pumped laser emitting 532 nm wavelength radiation with a Hoya U340 filter at 90% power, however, as expected from the multi grain results most grains were very dim, and therefore impede further single grain quartz OSL analysis.

Similar protocol as outlined in Table 2.2 was used for feldspar single grain analysis; post IR-$IRSL_{225}$ stimulation for potassium feldspar grains was performed using a 150 mW 830 nm IR laser filtered with the combination of RG780 (Bøtter-Jensen et al., 2003), Corning/Kopp 7-59, and Schott BG39 transmitting 320-460 nm for 1.6 s. The preceding IR_{50} measurement step was similar to a multi-grain analysis by stimulating all grains on the disc simultaneously with infrared LEDs. The number of accepted grains (after screening for recycling and recuperation ratios, oversaturated signals, very slow decaying signals or badly-fit growth curves) for the first analyzed sample (WW1803) was less than 10%, therefore, to enhance the outcome a hand-magnet was used to separate the remaining magnetic grains and improved the accepted data to ~40%. The single grain results were modeled with the central age model (CAM) (Galbraith et al.,

1999), minimum age model (MAM) (Galbraith et al., 1999) and finite mixture model (FMM) (Galbraith, 2005) utilizing the luminescence software package (Burow, 2018) in R (see section 2.5.11). Single grain kernel density estimate (KDE) diagrams and radial plots are presented in Appendix B.

2.5.6 - Environmental dose rate

For the twelve tube samples, dried exposed ends of each sample (~30 ml) were pulverized into fine powder in a shatter box using a tungsten carbide ring and puck mill. Then ~10 g of powder from each sample was sent to SGS Canada Inc. in Ontario, Canada, for ICP-AES/ -MS analysis to determine the elemental concentrations of K, Th, U (Table 2.3) and Rb. Considering the heterogeneous environment in the two fanglomerate samples (composed of fine sand smaller than 90 μm up to clasts as big as ~5 cm in diameter), 3 portions of each sample (>2 mm, <2 mm, and a mixture of the two sizes) was separately pulverized and then sent for ICP - AES/ -MS analysis (Table 2.4). 2 mm grain size was selected to separate the very coarse sand from the rest of the clasts. In addition, these two samples were analyzed by means of high-resolution gamma spectrometry for >2 mm and <2 mm proportions (Table 2.4). This analysis was performed at the OSL lab in Prairie Research Institute of the Illinois State Geological Survey.

The environmental dose rate was calculated utilizing the DRAC dose rate calculator (Durcan et al., 2015). For dose-rate calculations, radionuclide conversion factors from Liritzis et al. (2013) were used. Brennan et al. (1991) was selected for the grain size attenuation factors for the alpha dose rate; and the grain size attenuation factors for the beta dose rate was calculated after Guerin et al. (2012). For feldspar dose rate calculations, the internal potassium was

assumed to be 12.5% ± 0.5% (Huntley and Baril, 1997). As mentioned earlier, our potassium feldspar samples were not etched. Therefore, alpha track efficiency value and uncertainty was assumed to be 0.15 ± 0.05 for coarse-grained K-feldspar (Balescu and Lamothe, 1994). To calculate the cosmic dose-rate, DRAC uses the calculation protocol based on Prescott and Hutton (1994). As mentioned in section 2.5.2, samples were dried in a 50°C oven to record field moisture. Water content was calculated based on present day water content. Most of our samples are almost dry (water content < 1%). Results for each sample is shown in Table 2.3. Detailed dose rate analysis for the two fanglomerate samples is presented in Table 2.4. In the mix dose rate calculation, alpha and beta dose rates come only from <2 mm proportion, but both proportions contribute to gamma dose rate calculation (normalized by weight). Since we are dealing with K-feldspar, the internal K will reduce the effect of this heterogeneity in the fanglomerate environment as well.

For samples WW1801, WW1803 and MC1807 the dose rate was also calculated for 212-250 μm grain size used in single grain analysis.

Table 2.3 Sample radioactive nuclide concentrations, and dose rate.

Sample	Grain size[a] (μm)	Water content[b] (%)	U[c] (ppm)	Th[c] (ppm)	K[c] (%)	Rb[c] (ppm)	Cosmic dose rate[d] (Gy/ka)	Total dose rate (Gy/ka)
WW1801	125-170	2.53	2.53 ± 0.13	17.5 ± 0.88	2.7 ± 0.14	135 ± 6.75	0.07 ± 0.007	5.40 ± 0.18
WW1802	125-170	0.89	1.40 ± 0.07	13.3 ± 0.67	2.7 ± 0.14	103 ± 5.15	0.07 ± 0.007	4.82 ± 0.16
WW1803[*]	125-170	0.15	1.71 ± 0.09	15.7 ± 0.79	3 ± 0.15	118 ± 5.9	0.07 ± 0.007	5.45 ± 0.18
WW1804	125-170	2.72	2.82 ± 0.14	23 ± 1.15	2.6 ± 0.13	112 ± 5.6	0.06 ± 0.006	5.81 ± 0.20
WW1805	125-170	4.17	1.49 ± 0.07	18.3 ± 0.92	2.3 ± 0.12	81.4 ± 4.07	0.19 ± 0.019	4.82 ± 0.17
MC1801	125-170	0.37	2.17 ± 0.11	15.3 ± 0.77	2.9 ± 0.15	99.3 ± 4.97	0.03 ± 0.003	5.40 ± 0.18
MC1802	90-125	0.54	1.22 ± 0.06	5.2 ± 0.26	2 ± 0.10	69.6 ± 3.48	0.22 ± 0.022	3.48 ± 0.12
MC1803	125-170	0.24	1.47 ± 0.07	14.4 ± 0.72	2.5 ± 0.13	97.1 ± 4.86	0.17 ± 0.017	4.86 ± 0.16
MC1804	125-170	0.19	2.08 ± 0.10	14.4 ± 0.72	2.8 ± 0.14	86.4 ± 4.32	0.21 ± 0.021	5.38 ± 0.17
MC1805	125-170	0.54	2.47 ± 0.12	13.7 ± 0.69	2.5 ± 0.13	107 ± 5.35	0.18 ± 0.018	5.08 ± 0.16
MC1806	125-170	0.80	2.43 ± 0.12	17.4 ± 0.87	2.9 ± 0.15	105 ± 5.25	0.19 ± 0.019	5.78 ± 0.19
MC1807[*]	125-170	0.19	1.7 ± 0.09	9.5 ± 0.48	3.5 ± 0.18	129 ± 6.45	0.03 ± 0.003	5.39 ± 0.18

Conversion factors based on Liritzis et al. 2013.
[a]For samples WW1801, 03 and MC1807, dose rate has also been calculated for 212-250 μm grain size for single grain data.
[b]Water content uncertainty is assumed to be 25%.
[c]Elemental concentrations from ICP -AES/-MS data, SGS Canada, Ontario, CA.
[d]Cosmic dose rate calculations according to Prescott and Hutton (1994).
[*]Measured based on the pulverized mixture of the >2 mm and <2 mm grain sizes of the sample.

Table 2.4 Detailed dose rate analysis of the two fanglomerate samples.

Sample	Percentage (%)	U (ppm)	Th (ppm)	K (%)	Rb (ppm)	Total dose rate (Gy/ka)
WW1803 (>2mm)	85.08	1.52 ± 0.08	6.8 ± 0.34	1.4 ± 0.07	69.4 ± 3.47	3.03 ± 0.11
WW1803 (<2mm)	14.92	1.57 ± 0.08	14.2 ± 0.71	2.7 ± 0.14	102 ± 5.1	4.98 ± 0.17
WW1803 (mix)[a]	100					4.88 ± 0.17[p]
WW1803 (>2mm)[b]	85.08	2.43 ± 0.03	12.36 ± 0.17	1.93 ± 0.03	-	4.29 ± 0.12
WW1803 (<2mm)[b]	14.92	1.89 ± 0.02	14.25 ± 0.17	2.72 ± 0.03	-	5.09 ± 0.12
WW1803 (mix)[a, b]	100					5.06 ± 0.12[p]
MC1807 (>2mm)	67	1.49 ± 0.07	11.4 ± 0.57	3.6 ± 0.18	111 ± 5.55	5.59 ± 0.19
MC1807 (<2mm)	33	1.62 ± 0.08	11.8 ± 0.59	3.4 ± 0.17	106 ± 5.3	5.46 ± 0.18
MC1807 (mix)[a]	100					5.46 ± 0.19[p]
MC1807 (>2mm)[b]	67	1.58 ± 0.04	12.86 ± 0.25	3.44 ± 0.05	-	5.59 ± 0.13
MC1807 (<2mm)[b]	33	1.56 ± 0.02	9.86 ± 0.11	3.44 ± 0.03	-	5.32 ± 0.11
MC1807 (mix)[a, b]	100					5.37 ± 0.12[p]

[a]Mix dose rate calculation: alpha and beta dose rate from <2 mm proportion and gamma dose rate from both proportions.
[b]Results of high-resolution gamma spectrometry.
[p]Preferred dose rate for each sample is the average between the two values of mix dose rate calculated based on ICP -AES/-MS and high-resolution gamma spectrometry radionuclide concentrations.

2.5.7 - Residual Dose

Residual dose is the likely amount of luminescence signal that remains in a sample after daylight bleaching before burial and is expected to be more significant for high-energy depositional environments like fluvial deposits, since grains have less time to be exposed to sunlight. (This issue is expected to be more critical for fanglomerates as they may have deposited with debris flows that make light penetration difficult.). Residual dose measurement is a test trying to estimate the amount of this residual signal in the sample; however, the exact duration for bleaching a sample in sunlight is only an estimate based on the assumed depositional environment and hence residual dose measurement could be a significant source of uncertainty. Residual dose measurement is important because if not considered can lead to age overestimations. Feldspar IRSL signal bleaches more slowly by sunlight than the quartz signal (Thomsen et al., 2008). Moreover, post-IR IRSL signal is more difficult to bleach compared to IRSL (Poolton et al., 2002). In order to measure the level of residual dose, i.e. bleaching of the natural dose, in our samples, two or three 1 mm aliquots (same grain size used for multi grain De measurements) of each sample were exposed to sunlight outside in a sunny day for only an hour considering the relatively high energy transportation and depositional environment in alluvial fan settings (see section 2.4). Residual dose was measured using the protocol outlined in Table 2.2. The $pIRIR_{225}$ residual dose range from 4.7 ± 0.3 Gy to 28.8 ± 2.3 Gy, whereas the IR_{50} residual doses are much less significant and range from 0.7 ± 0.1 Gy to 3.7 ± 0.7 Gy. Residual doses were subtracted from $pIRIR_{225}$ De values before age calculation. Results are shown in Table 2.5; values are an average between the aliquots.

2.5.8 - Dose Recovery

The dose recovery test is used to determine whether a protocol is capable of accurately measuring a known given dose (e.g. Murray and Wintle, 2003; Buylaert et al., 2012). For this purpose, three aliquots from each sample were bleached outside in sunlight for one hour and then irradiated with a known dose equal to each sample's average De. Table 2.6 shows the results before subtracting the residual dose. Results after subtracting the residual dose are represented in Figs 2.15 and 2.16. For the high-temperature protocol ($pIRIR_{225}$) all samples except for WW1803 and MC1806 were able to recover the given dose within a 10% acceptance threshold. For the IR_{50}, sample MC1801 could not recover the given dose. Dose recovery issues have been observed by others (e.g. Stevens et al., 2011; Thiel et al., 2011; Buylaert et al., 2012; Murray et al., 2014); however, according to Buylaert et al. (2012) poor dose recovery ratios for feldspar does not necessarily mean inaccurate De measurements. Furthermore, dose recovery is test-dose size dependent and pIRIR protocols usually work best when the test dose is 30-50 % of the measured dose; however, this value for test dose is also sample dependent (Buylaert pers. comm., 2019).

2.5.9 - Fading Rates

Anomalous fading was first recognized by Wintle in 1973 for feldspar thermoluminescence. This phenomenon is known to be the result of the quantum mechanical tunneling of electrons (Visocekas, 1985; Visocekas et al., 1994). Anomalous fading is approximated by a logarithmic decay, therefore, the fading rate (g value) is expressed as the percentage of signal lost for a storage period of one decade (Aitken, 1985; Buylaert, 2007).

After being used for measuring De, aliquots were bleached; the SAR cycle was then repeated several times using a regeneration dose of ~80 or ~100 Gy with varying storage periods (ranged from 1 h to 24 h) after the regeneration doses. Aliquots were preheated immediately after irradiation according to Auclair et al. (2003). Fading rates were assessed for seven samples using five or six aliquots for each. Results show that the anomalous fading is negligible for $pIRIR_{225}$, but are significant for IR_{50} (Table 2.7). Error on individual aliquots have the minimum of 0.96 and maximum of 1.71, hence the $pIRIR_{225}$ fading rates are almost within the errors and fading corrections are not applied for this protocol.

Table 2.5 Residual dose for the $pIRIR_{50}$ and IR_{50} protocols after bleaching the aliquots for an hour outside in sunlight. These residual dose values are approximately 3-6 % of the De for each sample.

Sample	Number of aliquots	$pIRIR_{225}$ (Gy)	IR_{50} (Gy)
WW1801	2	13.2 ± 1.9	1.9 ± 0.1
WW1802	2	13.5 ± 2.0	1.1 ± 0.7
WW1803	2	25.1 ± 3.0	3.7 ± 0.7
WW1804	3	21.1 ± 1.4	2.8 ± 0.2
WW1805	2	21.0 ± 5.3	3.0 ± 0.7
MC1801	2	16.0 ± 1.6	2.3 ± 0.2
MC1802	3	28.8 ± 2.3	3.6 ± 0.3
MC1803	3	4.7 ± 0.3	0.7 ± 0.1
MC1804	3	13.7 ± 0.7	2.4 ± 0.3
MC1805	3	17.8 ± 1.9	2.2 ± 0.3
MC1806	2	5.8 ± 2.6	1.7 ± 0.3
MC1807	2	15.1 ± 1.6	2.6 ± 0.3

Table 2.6 Dose recovery test for the $pIRIR_{50}$ and IR_{50} protocols. Given dose is based on the average De recorded for each sample. Results are the average measured/given (M/G) ratios for three aliquots, before and after (indicated by the $_R$ subscript) subtracting the residual dose.

Sample	Given dose (Gy)	$pIRIR_{225}$ (M/G)	$pIRIR_{225}$ $(M/G)_R$	IR_{50} (M/G)	IR_{50} $(M/G)_R$
WW1801	385.8	1.10 ± 0.02	1.07 ± 0.02	1.01 ± 0.01	1.00 ± 0.01
WW1802	321.5	1.02 ± 0.03	0.98 ± 0.03	1.03 ± 0.04	1.02 ± 0.04
WW1803	385.8	0.95 ± 0.02	0.90 ± 0.02	1.04 ± 0.02	1.03 ± 0.02
WW1804	385.8	1.04 ± 0.02	0.99 ± 0.02	1.04 ± 0.01	1.04 ± 0.01
WW1805	448	0.98 ± 0.02	0.93 ± 0.02	1.01 ± 0.04	1.00 ± 0.04
MC1801	385.8	1.06 ± 0.02	1.02 ± 0.02	1.12 ± 0.02	1.11 ± 0.02
MC1802	900.2	1.02 ± 0.01	0.99 ± 0.01	1.06 ± 0.05	1.03 ± 0.05
MC1803	128.6	0.98 ± 0.04	0.94 ± 0.04	1.03 ± 0.03	1.02 ± 0.03
MC1804	128.6	1.05 ± 0.01	0.95 ± 0.01	1.04 ± 0.03	1.02 ± 0.03
MC1805	321.5	1.04 ± 0.01	0.99 ± 0.01	0.99 ± 0.02	0.98 ± 0.02
MC1806	19.2	1.18 ± 0.05	0.88 ± 0.05	1.01 ± 0.03	0.92 ± 0.03
MC1807	321.5	1.05 ± 0.01	1.00 ± 0.01	0.99 ± 0.01	0.98 ± 0.01

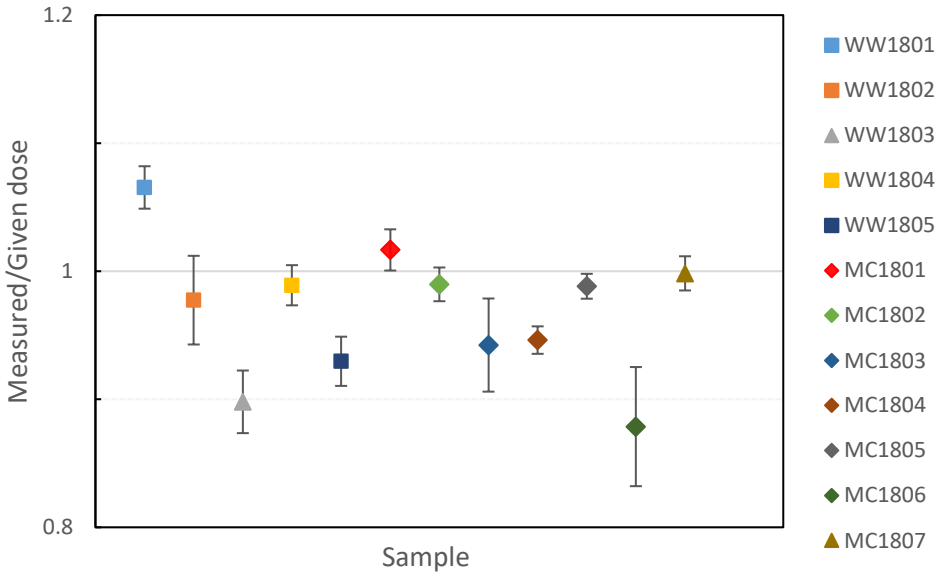

Figure 2.15 Dose recovery results for the pIRIR$_{225}$ protocol after subtracting the residual dose. Given dose is based on the average De for each sample (Table 2.6). Each point represents the average of three aliquots. Gray dashed lines show the 10% acceptance threshold.

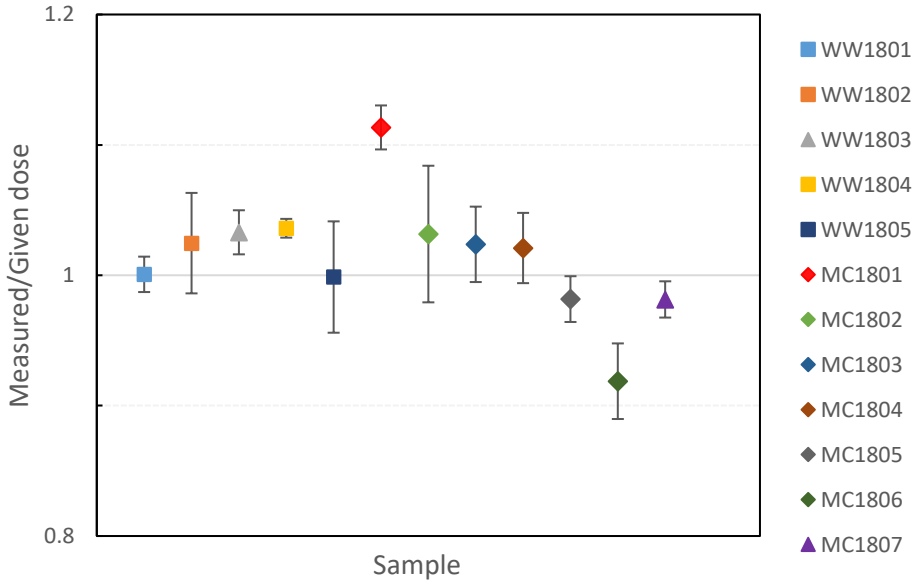

Figure 2.16 Dose recovery results for the IR$_{50}$ protocol after subtracting the residual dose. Each point represents the average of three aliquots. Gray dashed lines show the 10% acceptance threshold.

Table 2.7 Fading rates measured for seven samples. Values are average between five or six aliquots.

Sample	g-value (%/decade) $pIRIR_{225}$	g-value (%/decade) IR_{50}
WW1801	2.8 ± 0.69	9.3 ± 2.18
WW1803	3 ± 0.65	8.0 ± 0.41
WW1804	2.3 ± 0.78	7.5 ± 1.37
MC1803	2.5 ± 1.74	8.8 ± 2.42
MC1804	2.5 ± 0.77	9.4 ± 1.25
MC1805	2.6 ± 0.83	7.3 ± 1.77
MC1807	2.4 ± 0.81	5.8 ± 1.29

2.5.10 - Multigrain Equivalent Dose (De) Modeling

The equivalent dose (De) value for each sample was calculated using both central age model (CAM) (Galbraith et al., 1999) and minimum age model (MAM) (Galbraith et al., 1999) with luminescence software package (Burow, 2018) in R. Table 2.8 represents the results for each sample. Number of aliquots used to carry out the De for each sample is indicated and the results are from the aliquots with recycling ratios within 10% of unity. Overdispersion percentage (OD %) for CAM and the significance (P0) for MAM are shown. P0 represents the proportion of the data used to produce De in MAM. Radial plots and kernel density estimates (KDE) diagrams are presented in Appendix A.

Samples MC1803 and MC1804 have considerable overdispersion within their De values and increasing the number of aliquots could not help resolving this issue. Due to the high possibility of bioturbation (especially in sampling location MC1804 due to the presence of roots in nearby sediments) and the fact that MAM is susceptible toward small De values, we analyzed

these two samples separately by removing the very small De values (compared to the population) (Table 2.9). For sample MC1803, by removing the small De values the significance (P0) in the MAM was not increased. For this reason, we preferred the initial De value based on the CAM. On the other hand, P0 increased for sample MC1804 so the preferred De is according to the MAM in second iteration.

The same analysis was performed for IR_{50} results (Tables 2.10 and 2.11). Preferred De values are shown for each sample.

2.5.11 - Single Grain De Modeling

Tables 2.12, 2.13 and 2.14 show the results of finite mixture models (FMM) (Galbraith, 2005) performed with luminescence software package (Burow, 2018) in R for samples WW1801, WW1803 and MC1807 (single grain data). FMM is useful when the number of aliquots is large and may represent all possible components in the data: well-bleached, partially-bleached, and bioturbated grains. In these tables, n shows the number of grains accepted in each case for De determination, n.comp is the number of components used in each FMM, BIC is the Bayesian Information Criterion (Schwartz, 1978) and P shows the proportion of each De value in the model. In each case, different number of components and different σ_b (characterizes overdispersion in a sample if aliquots are well bleached) values (10%, 20%, 30%) were examined since it is difficult to evaluate σ_b in sediment mixtures (Galbraith and Roberts, 2012). BIC decreases as more components are added to the model, but will start increasing when the extra components are redundant (Galbraith, 2005; Galbraith and Roberts, 2012). Therefore, the best fit is evaluated based on maximum likelihood and minimum BIC. For each σ_b value, the number of components is increased until the BIC starts increasing.

For sample WW1801 (Table 2.12), the best fit comes from $\sigma_b = 0.2$ with two or three number of components (fit numbers 3 and 4). However, with the three number of components we can see the possibility of mixing light-exposed grains with the majority of grains (P = 0.52). For this reason, De_2 in fit number 4 (252.32 ± 28.20 Gy) is the preferred De value.

For sample WW1803 (Table 2.13), numbers 6 through 9 are the best fits according to the likelihood and BIC values. When there is three number of components in the model (6 and 9), the middle De value (De_2) with the highest population (P= 0.48 or 0.46) is in the same range, however, with much more significant error when $\sigma_b = 0.3$. De_2 in fit number 6 (258.57 ± 14.65 Gy) is then used in age calculation.

For sample MC1807 (Table 2.14), numbers 8 and 10 are the best fits according to the likelihood and BIC values with $\sigma_b = 0.2$ and 0.3. In fit number 8, there are four components and De_3 and De_4 have the highest proportions (214.24 ± 14.31 Gy, P= 0.42; 368.47 ± 15.74 Gy, P = 0.43). In number 10, De_3 has the highest population (310.57 ± 14.05 Gy, P = 0.68). In this case it is more challenging to decide which De value is preferable for age calculations and we will compare all these three values.

2.5.12 - Age Calculations

For each sample the age is calculated based on the preferred De from $pIRIR_{225}$ results (see Tables 2.8 and 2.9). Fading rates are not applied to $pIRIR_{225}$ results, but residual doses are subtracted (Table 2.15). Where fading rates have been measured, age is also calculated from IR_{50} results and compared with $pIRIR_{225}$ results (Table 2.15). Due to the high fading rates and their significant error, ages derived from IR_{50} results have large errors that makes these results

unusable. Ages for samples WW1801, WW1803 and MC1807 are also assessed based on single grain De results (Table 2.15).

Table 2.8 Equivalent dose (De) modeling for $pIRIR_{225}$ results. For each sample the De is modeled based on the central age model (CAM) and minimum age model (MAM) with the luminescence software package in R program. n indicates the number of aliquots used for each sample. OD is the overdispersion in the CAM model and P0 is the significance in the MAM model.

Sample	n	De (Gy) CAM	OD %	De (Gy) MAM	P0
WW1801	27	348.86 ± 20.56	29.68	282.35 ± 30.95[p]	0.29
WW1802	22	343.46 ± 23.72	31.58	256.04 ± 32.15[p]	0.10
WW1803	24	372.11 ± 17.84	22.32	355.09 ± 34.50[p]	0.79
WW1804	15	390.17 ± 15.69[p]	14.94	338.99 ± 25.43	0.02
WW1805	10	486.32 ± 31.62[p]	18.77	486.72 ± 58.59	1
MC1801	20	442.75 ± 23.98	22.49	401.98 ± 46.25[p]	0.33
MC1802	6	899.59 ± 28.43[p]	3.63	899.98 ± 51.75	1
MC1803[*]	26	87.80 ± 16.02[p]	92.41	26.29 ± 4.18	0.12
MC1804[*]	31	135.05 ± 18.91	77.72	30.35 ± 5.37	0.01
MC1805	15	318.61 ± 16.44[p]	18.87	318.68 ± 29.41	1
MC1806	8	17.97 ± 3.35[p]	52.45	9.35 ± 2.08	0.11
MC1807	24	327.20 ± 21.70[p]	31.68	240.07 ± 29.74	0.02

[*]See the detailed analysis in Table 2.9.
[p]The preferred De for age calculation.

Table 2.9 Detailed analysis of samples MC1803 and MC1804 based on $pIRIR_{225}$ results. Outliers were removed in order to decrease the overdispersion and reliability of the MAM results.

Sample	n	De (Gy) CAM	OD %	De (Gy) MAM	P0
MC1803	20	125.79 ± 20.78	73.49	47.47 ± 7.58	0.11
MC1803	16	162.59 ± 24.12	58.84	77.13 ± 14.80	0.06
MC1804	22	207.01 ± 16.13	36.01	142.25 ± 18.83[p]	0.08

[p]The preferred De for age calculation.

Table 2.10 Equivalent dose (De) modeling for IR_{50} results. For each sample the De is modeled based on the central age model (CAM) and minimum age model (MAM) with the luminescence software package in R program. n indicates the number of aliquots used for each sample. OD is the overdispersion in the CAM model and P0 is the significance in the MAM model.

Sample	n	De (Gy) CAM	OD %	De (Gy) MAM	P0
WW1801	28	128.11 ± 7.96[p]	32.18	94.90 ± 11.53	0.09
WW1802	22	141.46 ± 8.08	26.04	128.74 ± 12.82	0.69
WW1803	24	144.34 ± 8.38	27.84	135.97 ± 14.22[p]	0.84
WW1804	15	185.12 ± 13.66[p]	27.79	147.86 ± 20.89	0.10
WW1805	10	174.36 ± 9.33	15.34	174.30 ± 17.92	1
MC1801	21	255.45 ± 23.94	42.39	151.71 ± 20.74	0.07
MC1802	6	396.59 ± 22.91	11.65	371.19 ± 39.57	0.14
MC1803[*]	25	41.24 ± 6.20	73.91	15.33 ± 2.50	0.07
MC1804[*]	31	39.77 ± 5.72	79.43	9.73 ± 2.00	0.01
MC1805	15	108.12 ± 4.45[p]	14.90	107.99 ± 8.82	1
MC1806	8	7.41 ± 1.37	51.68	3.94 ± 0.92	0.09
MC1807[*]	23	163.33 ± 15.84	46.09	92.47 ± 14.51	0.01

[*]See the detailed analysis in Table 2.9.
[p]The preferred De for age calculation.

Table 2.11 Detailed analysis of samples MC1803, MC1804 and MC1807 based on IR_{50} results. Outliers were removed in order to decrease the overdispersion and reliability of the MAM results.

Sample	n	De (Gy) CAM	OD %	De (Gy) MAM	P0
MC1803	18	58.50 ± 7.75	55.36	41.57 ± 5.27[p]	0.53
MC1804	28	46.86 ± 5.71	64.05	19.82 ± 2.86	0.07
MC1804	22	57.39 ± 6.26	51.76	29.45 ± 4.46	0.03
MC1804	19	67.63 ± 6.50	41.32	51.84 ± 7.19[p]	0.44
MC1807	21	177.79 ± 15.15	38.56	141.06 ± 16.53[p]	0.52

[p]The preferred De for age calculation.

Table 2.12 Finite mixture modeling (FMM) for sample WW1801. n shows number of grains, n.comp is the number of components used in each FMM model, BIC is the Bayesian Information Criterion and P shows the proportion of each equivalent dose (De).

N	n	n.comp	σ_b	likelihood	BIC	De_1	P	De_2	P	De_3	P
1	125	2	0.1	-81.27	177.02	220.47 ± 4.55	0.62	409.26 ± 14.63	0.38		
2	125	3	0.1	-51.51	127.16	185.02 ± 8.43	0.26	269.29 ± 9.96	0.48	467.95 ± 18.63	0.25
3	125	2	0.2	-50.28	115.04	230.30 ± 7.41	0.68	430.65 ± 26.21	0.32		
4	125	3	0.2	-49.55	123.24	196.30 ± 36.79	0.2	252.32 ± 28.20[p]	0.52	445.87 ± 30.39	0.28
5	125	2	0.3	-52.92	120.34	247.14 ± 13.43	0.75	413.52 ± 52.86	0.25		

[p]The preferred De for age calculation.

Table 2.13 Finite mixture modeling (FMM) for sample WW1803. n shows number of grains, n.comp is the number of components used in each FMM model, BIC is the Bayesian Information Criterion and P shows the proportion of each equivalent dose (De).

N	n	n.comp	σ_b	likelihood	BIC	De_1	P	De_2	P	De_3	P	De_4	P	De_5	P
1	232	2	0.1	-409.70	835.73	162.66 ± 5.03	0.44	361.21 ± 12.18	0.56						
2	232	3	0.1	-235.05	497.33	130.30 ± 2.89	0.24	239.34 ± 6.69	0.39	427.87 ± 12.01	0.37				
3	232	4	0.1	-196.08	430.28	124.92 ± 4.10	0.2	214.56 ± 7.99	0.31	335.12 ± 11.14	0.32	547.07 ± 20.79	0.15		
4	232	5	0.1	-170.25	389.51	95.48 ± 6.08	0.06	146.87 ± 5.46	0.19	229.26 ± 6.31	0.29	344.63 ± 11.14	0.30	552.41 ± 21.67	0.15
5	232	2	0.2	-211.82	439.99	161.57 ± 6.21	0.43	362.71 ± 12.87	0.57						
6	232	3	0.2	-176.48	380.20	132.80 ± 5.84	0.25	258.57 ± 14.65[P]	0.48	464.41 ± 32.22	0.27				
7	232	4	0.2	-172.92	383.96	96.17 ± 18.64	0.05	152.70 ± 16.36	0.25	274.52 ± 17.09	0.47	484.83 ± 35.19	0.23		
8	232	2	0.3	-176.14	368.62	161.87 ± 9.86	0.40	351.08 ± 16.68	0.60						
9	232	3	0.3	-173.14	373.51	140.29 ± 14.22	0.24	256.88 ± 41.50	0.46	422.17 ± 54.56	0.30				

[P]The preferred De for age calculation.

Table 2.14 Finite mixture modeling (FMM) for sample MC1807. n shows number of grains, n.comp is the number of components used in each FMM model, BIC is the Bayesian Information Criterion and P shows the proportion of each equivalent dose (De).

N	n	n.comp	σ_b	likelihood	BIC	De_1	P	De_2	P	De_3	P	De_4	P	De_5	P	De_6	P
1	231	2	0.1	-557.13	1130.60	122.53 ± 2.83	0.26	297.00 ± 3.96	0.74								
2	231	3	0.1	-311.41	650.02	52.24 ± 2.72	0.04	165.05 ± 3.48	0.36	330.04 ± 5.54	0.60						
3	231	4	0.1	-207.47	453.03	41.84 ± 2.36	0.03	124.40 ± 3.87	0.16	217.57 ± 5.35	0.39	373.59 ± 7.65	0.43				
4	231	5	0.1	-189.44	427.87	23.74 ± 3.03	0.01	59.88 ± 3.53	0.03	133.78 ± 4.79	0.17	224.01 ± 6.90	0.38	377.40 ± 8.71	0.41		
5	231	6	0.1	-168.87	397.61	23.51 ± 2.60	0.01	50.48 ± 3.38	0.02	103.12 ± 7.16	0.07	167.09 ± 12.71	0.22	257.56 ± 19.27	0.37	407.32 ± 21.90	0.31
6	231	2	0.2	-262.91	542.15	115.84 ± 6.06	0.23	296.40 ± 7.00	0.77								
7	231	3	0.2	-185.56	398.32	48.07 ± 5.50	0.04	167.30 ± 7.84	0.37	333.89 ± 10.78	0.59						
8	231	4	0.2	-168.94	375.98	41.11 ± 3.83	0.03	120.64 ± 10.82	0.12	214.24 ± 14.31[p]	0.42	368.47 ± 15.74[p]	0.43				
9	231	2	0.3	-190.75	397.84	83.26 ± 11.49	0.11	272.24 ± 8.20	0.89								
10	231	3	0.3	-168.50	364.22	41.94 ± 6.18	0.03	159.12 ± 13.63	0.29	310.57 ± 14.05	0.68						
11	231	4	0.3	-166.47	371.47	21.78 ± 6.60	0.01	59.40 ± 13.13	0.3	166.89 ± 16.27	0.3	314.51 ± 15.53	0.6				

[p]The preferred De for age calculation.

Table 2.15 Calculated ages based on preferred De values of the $pIRIR_{225}$ and IR_{50} data. For $pIRIR_{225}$ residual doses are subtracted and fading rates are applied. For IR_{50} residual doses are not subtracted, but fading rates are applied.

Sample	Dose rate (Gy/ka)	De (Gy) $pIRIR_{225}$	Age[a] (ka)	De (Gy) IR_{50}	Age[b] (ka)
WW1801	5.40 ± 0.18	282.35 ± 30.95 (MAM)	65.07 ± 9.40	128.11 ± 7.96 (CAM)	77.83 ± 31.54
WW1801*	5.48 ± 0.15	280.77 ± 9.32 (CAM)	63.73 ± 5.87		
WW1801*	5.48 ± 0.15	252.32 ± 28.20 (FMM)	56.91 ± 8.28		
WW1802	4.82 ± 0.16	256.04 ± 32.15 (MAM)	65.76 ± 10.46	128.74 ± 12.82 (MAM)	88.89 ± 37.12
WW1803	4.97 ± 0.21	355.09 ± 34.50 (MAM)	88.76 ± 12.22	135.97 ± 14.22 (MAM)	70.27 ± 10.80
WW1803*	5.08 ± 0.18	257.63 ± 8.70 (CAM)	61.03 ± 5.75		
WW1803*	5.08 ± 0.18	258.57 ± 14.65 (FMM)	61.27 ± 6.55		
WW1804	5.81 ± 0.20	390.17 ± 15.69 (CAM)	78.81 ± 8.04	185.12 ± 13.66 (CAM)	75.47 ± 26.76
WW1805	4.82 ± 0.17	486.32 ± 31.62 (CAM)	122.68 ± 11.81	174.36 ± 9.33 (CAM)	94.52 ± 26.80
MC1801	5.40 ± 0.18	401.98 ± 46.25 (MAM)	90.62 ± 13.96	151.71 ± 20.74 (MAM)	72.14 ± 21.80
MC1801	5.40 ± 0.18	442.75 ± 23.98 (CAM)	100.24 ± 11.23	255.45 ± 23.94 (CAM)	125.23 ± 37.37
MC1802	3.48 ± 0.12	899.59 ± 28.43 (CAM)	320.17 ± 33.82	396.59 ± 22.91 (CAM)	322.19 ± 104.78

MC1803	4.86 ± 0.16	87.80 ± 16.02 (CAM)	21.53 ± 5.93	41.57 ± 5.27 (MAM)	23.39 ± 29.75
MC1804	5.38 ± 0.17	142.25 ± 18.83 (MAM)	30.13 ± 5.20	51.84 ± 7.19 (MAM)	29.67 ± 14.22
MC1805	5.08 ± 0.16	318.61 ± 16.44 (CAM)	75.83 ± 8.68	108.12 ± 4.45 (CAM)	48.05 ± 21.41
MC1806	5.78 ± 0.19	17.97 ± 3.35 (CAM)	2.60 ± 0.93	7.41 ± 1.37 (CAM)	2.74 ± 0.73
MC1807	5.42 ± 0.22	327.20 ± 21.70 (CAM)	72.19 ± 8.75	163.33 ± 15.84 (CAM)	55.49 ± 13.95
MC1807	5.42 ± 0.22	240.07 ± 29.74 (MAM)	51.96 ± 8.58	141.06 ± 16.53 (MAM)	47.75 ± 12.33
MC1807*	5.54 ± 0.21	241.04 ± 8.66 (CAM)	51.04 ± 5.36		
MC1807*	5.54 ± 0.21	214.24 ± 14.31 (FMM)	44.96 ± 5.45		
MC1807*	5.54 ± 0.21	368.47 ± 15.74 (FMM)	79.99 ± 8.63		

[a]Corrected age after subtracting the residual dose and applying the fading rate.
[b]Corrected age after applying the fading rate.
*Single grain results.

2.6 – Discussion

2.6.1 - Method Development

Based on our results from both multi grain and single grain analysis, quartz OSL signal is very dim impeding any equivalent dose (De) determination. This is probably due to the proximity of our sampling sites to new bedrock (igneous/ metamorphic sources) which means that quartz grains have not undergone many erosional/ depositional cycles (Lawson et al., 2012). Lawson et al. (2012) reported low quartz OSL sensitivity and poor characteristics for fluvial

sediment samples collected in the Coachella Valley close to Palm Springs and the Salton Sea. According to Lawson et al. (2012) this region is tectonically active and new bedrock is continuously being exposed through thrust faulting (e.g. in the San Gabriel Mountains) and normal faulting (associated with Basin and Range extension), providing fresh material to the surface, which is eroded, and rapidly fills subsiding basins before significant grain reworking is possible.

On the other hand, feldspar aliquots and most grains (from single grain analysis) were bright allowing age assessment for our samples. Ages were calculated using both $pIRIR_{225}$ and IR_{50} results. Fading rates in our samples are significant (Table 2.7) and were applied for both $pIRIR_{225}$ and IR_{50}. Residual doses were subtracted from $pIRIR_{225}$ De values before age calculation, but were not applied for IR_{50} since they are insignificant (Table 2.5). For most samples, the corrected IR_{50} ages are in accordance with $pIRIR_{225}$ results; however, their large errors impede any interpretations. For this reason, and the fact that our single grain data are only available for $pIRIR_{225}$, ages calculated based on the high-temperature IRSL are preferred.

While some previous work reported issues regarding dose recovery results of pIRIR protocols, our results show that the protocol is working well for most of our samples. The only samples that were not able to satisfactorily recover a dose were WW1803 and MC1806. However, a dose recovery test cannot solely be a rejection criterion for calculated De values (Buylaert, 2012).

Regarding the two fanglomerate samples, our results show the necessity of performing single grain analysis for fanglomerate dating as the probability of dating a fully bleached grain becomes higher. Additionally, based on the observations of Truelsen and Wallinga (2003), larger grain sizes tend to be better bleached in fluvial samples. We used 212-250 μm grain size for

single grain analysis that may have been better bleached compared to the 125-170 µm grain size used for multi grain analysis. Moreover, finite mixture modeling (FMM) of the single grain data help recognize the main population(s) of grains that demonstrate De value(s) with the highest proportion(s) in the data and hence clarify the best age model (CAM vs. MAM). Analyzing samples WW1801 (sand layer) and WW1803 (fanglomerate) with FMM, one population of De values with the highest proportion was distinguished. Nevertheless, analyzing sample MC1807 (fanglomerate) is more challenging since two populations of De values in FMM have almost an equal proportion. On the other hand, we could not sample any sand layer adjacent to MC1807 (the sand layer sample, MC1801 was collected ~20 m horizontally separated) which makes constraining the age of this sample more difficult.

Concerning the fanglomerate dose rate analysis, we performed ICP -AES/-MS analysis on >2 mm, <2 mm, and a mixture of the two materials. These samples were also analyzed utilizing high-resolution gamma spectrometry for >2 mm and <2 mm proportions. Comparing Th and K concentrations from the ICP -AES/-MS analysis and high-resolution gamma spectrometry, illustrate near homogeneous environment for the <2 mm proportions of the samples; however, the >2mm proportions are indicative of dose rate heterogeneity (i.e. different Th and K concentrations were measured from ICP -AES/-MS and high-resolution gamma spectrometry) that is most probably due to different lithologies. This heterogeneity in the >2 mm proportions became evident because we pulverized a few >2 mm clasts of each sample for ICP -AES/-MS analysis and used a second pulverized sub-sample for high-resolution gamma spectrometry analysis. The mixture of the two proportions (>2 mm and <2 mm) that was analyzed by means of ICP -AES/-MS shows different radionuclide concentrations compared to >2 mm and <2 mm proportions as a third pulverized sub-sample has been used. This issue can be solved by

pulverizing a rather large portion (e.g. 400 g) of the >2 mm proportion, mixing it thoroughly and extracting small portions (e.g. 10 g) for ICP -AES/-MS analysis; this way the mixture will be representative of almost all available lithologies in a sample. Since we did not follow this procedure, the final dose rate is then calculated based on the average of the ICP-AES/-MS and high-resolution gamma spectrometry results. Considering the penetration distance for alpha, beta and gamma dose rates, the alpha and beta dose rates were calculated based on the <2 mm proportion radionuclide concentrations and gamma dose rate was calculated based on the weighted mixture of the <2 mm and >2 mm proportions.

2.6.2 - Geological Implications

The three recognized alluvial fans (Fig 2.12) should have the same age based on their surface roughness and channel depth of incision. The matched alluvial fan (Fan 3) has an offset of ~600 m which is of the same order as the T2 alluvial fan along the Mission Creek fault. Woerd et al. (2006) proposed an offset of 565 ± 80 m for the TCN surface, which has an age of 35.5 ± 2.5 ka resulting in long term slip rate of 15.9 ± 3.4 mm/yr. Behr et al. (2010) recognized a minimum, a maximum and a preferred offset for the same fan to be 660 m, 980 m and 770 m, respectively; and the TCN surface age of the T2 alluvial fan to be between 45 and 54 ka which is also consistent with U-series dating of pedogenic carbonate clast coatings (Fletcher et al., 2010). Data from these studies yields a slip rate of 12.2 to 21.7 mm/yr along the Mission Creek fault at Biskra Palms (Behr et al., 2010). Based on the age of sample MC1805 (~75 ka), the minimum slip rate along the Mission Creek fault will be 7.0 ± 1.3 to 8.4 ± 1.4 mm/yr. OSL ages refer to sediment deposition in alluvial fans prior to offset and hence provide minimum slip rates that could suggest the slip rate along the Mission Creek fault is not changed at least along the length

between the T2 alluvial fan and our Fan 3. On the other hand, there is a possibility that the slip rate along the Mission Creek fault has slowed toward the northwest and the slip might then have been transferred to the Banning fault. The Banning fault is the principal fault from Biskra Palms further northwest (Keller et al., 1982; Yule and Sieh, 2003; Woerd et al., 2006). This is also in agreement with the observation of Gold et al. (2015), who suggested the onset of more significant slip transfer from the Mission Creek to the Banning strand to the northwest of Thousand Palms Canyon in Indio Hills area, over both long-term (Quaternary) and short-term (Holocene) timescales, based on the abrupt increase in topography, relief, stream incision, erosion and structural evidence. Furthermore, Owen et al. (2014) stated that none of the alluvial surfaces in the Mission Creek alluvial fan complex are offset by the Mission Creek fault (located to the northwest of Fan 3 along the Mission Creek fault, our WW1801-04 sampling location); therefore, there may have been little if any movement along this fault in San Bernardino mountains since at least marine isotope stage (MIS) 4.

As stated earlier, luminescence ages indicate age of deposition/ sedimentation of alluvial fans. Figure 2.17 demonstrates depositional alluvial fan ages in comparison with marine isotope stages. In alluvial fan fm4b (Owen et al., 2014) the age of our paleosol sample WW1804 (78.81 ± 8.04 ka) is consistent with the transition from MIS 5 to MIS 4 and the age of samples WW1801- 03 (65 ± 10 ka) are within the range of MIS 4, indicating that soil development occurred mostly during the interglacial period MIS 5 (WW1804 was taken from the top of the paleosol layer). However, alluvial fan formation happened during glacial period MIS 4 which is not in accordance with the arid alluvial fan model. Furthermore, our depositional age (65 ± 10 ka) is in agreement with the abandonment / incision age (63.0 ± 2.6 ka) from the TCN surface dating at this exposure (Owen et al., 2014), and may indicate fast deposition of this alluvial fan.

The age of sample WW1805 (122.68 ± 11.81) is within mid MIS 5 time, around the transition from interglacial to glacial sub-stage as well. Nonetheless, fan deposition in the locality of samples MC1801 and MC1807 (fanglomerate), with calculated ages of 100.24 ± 11.23 ka and 51.04 ± 5.36 ka, respectively, is within the interglacial periods MIS 5 (around the transition from glacial to interglacial sub-stage) and MIS 3 (around the transition from glacial MIS 4 to interglacial MIS 3). Sample MC1802 was collected from an older alluvial fan (Fig 2.6B) and is within time of interglacial MIS 9 (320.17 ± 33.82 ka). Analysis of sample MC1803 is difficult due to its high overdispersion (~90%); however, based on the preferred age its deposition was within mid glacial MIS 2 time (21.53 ± 5.93 ka). The deposition of sample MC1804 is within the late interglacial MIS 3 (30.13 ± 5.20 ka). MC1805 (75.83 ± 8.68 ka) is within the late interglacial MIS 5 to early glacial MIS 4. Sample MC1806 is our youngest sample (2.60 ± 0.93 ka) and is within Holocene (interglacial MIS 1). Since most of the alluvial fans in the Indio Hills area date to the glacial-interglacial transitions, the general pattern of alluvial fan formation in this area seems to confirm the arid alluvial fan model. However, for alluvial fans that are located along the Mission Creek fault in the Indio Hills area (samples MC1801-07), tectonic activity may have influenced alluvial fan deposition as well.

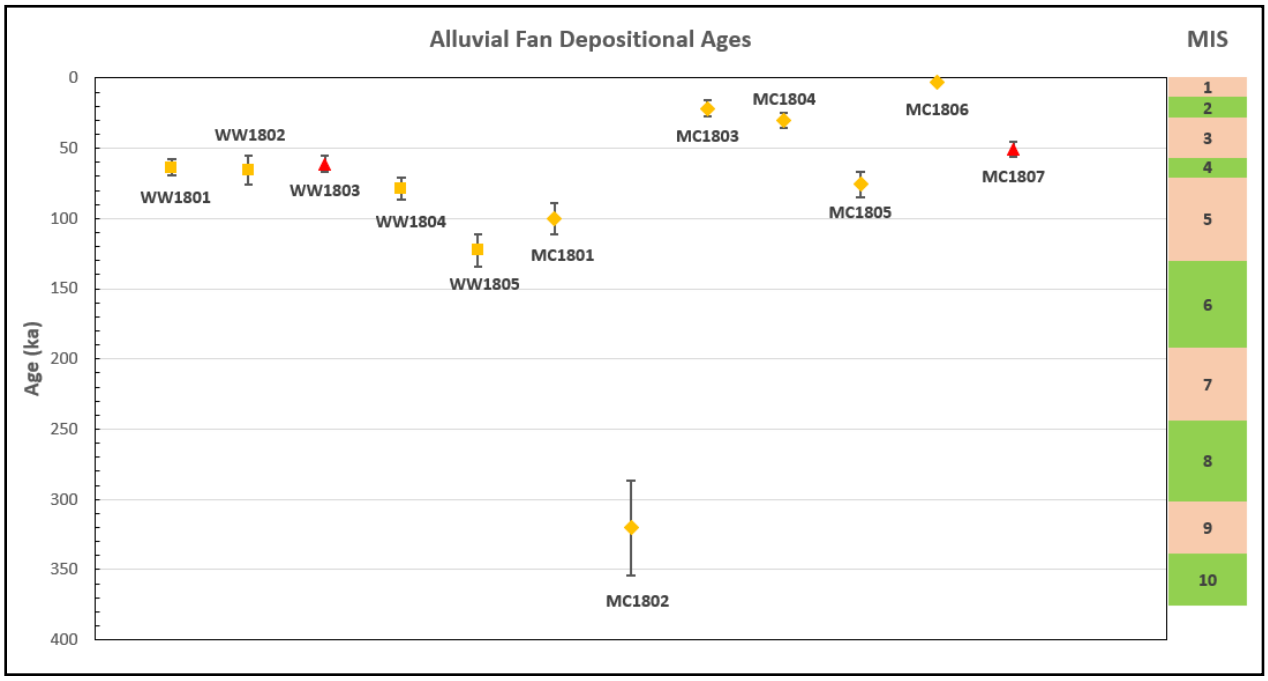

Figure 2.17 Schematic representation of luminescence alluvial fan ages in comparison with marine isotope stages (MIS). Marine isotope stages adapted from Lisiecki and Raymo (2005). The two fanglomerate samples are shown in red.

2.7 - Conclusions

Six main sites were sampled in the northern part of the Coachella Valley, some along the Mission Creek fault. Similar to some previous studies in southern California (e.g. Lawson et al., 2012; Roder et al., 2012; Rhodes, 2015) quartz OSL in our samples displayed very poor OSL characteristics, but feldspar IRSL was bright with good characteristics. Ages were calculated based on the De values derived from $pIRIR_{225}$ protocol. Regarding the two fanglomerate samples, single grain analysis and finite mixture modeling (FMM) seems essential for recognizing the main population of grains that demonstrate De values with the highest proportion(s) in the data and hence help clarify the best age model (CAM vs. MAM).

Samples WW1804 (paleosol), WW1805 and MC1805 have provided more robust age constraints compared to other samples due to their low overdispersion. Furthermore, the age of the two sand layer samples (WW1801 and WW1802) is in agreement with each other and with

the fanglomerate sample (WW1803) and all younger than the underneath paleosol (WW1804). These also confirm the TCN age at the surface of this fan.

Some of our samples (WW1801-05) confirm that the alluvial fans in this area were formed in the transition between interglacial to glacial periods. Nonetheless, samples MC1801-07 along the Mission Creek and Banning faults near in the Coachella Valley were formed during interglacial periods (MIS 3, MIS 5, MIS 9) and the Holocene.

The minimum slip rate along the Mission Creek fault based on our sample MC1805, is 7.0 ± 1.3 to 8.4 ± 1.4 mm/yr which is slower than its preferred geologic slip rate at Biskra Palms (14-17 mm/yr) (Behr et al., 2010) to the south of our location along the fault. This may mean that the slip along this fault has slowed toward north and thus transferred to the Banning fault.

Chapter 3 - Summary and Conclusions

Luminescence dating is amongst the geochronological methods that can date sediment deposition directly. This enables us to understand and interpret valuable environmental information such as climate history and tectonic activity. Our results show that alluvial fan formation in the Coachella Valley near Indio Hills mainly occurred during interglacial periods. Nevertheless, alluvial fans formed during the transition from interglacial to glacial in the north of the valley, east of San Bernardino Mountains. The minimum slip rate along the Mission Creek fault near Indio Hills is 7.0 ± 1.3 to 8.4 ± 1.4 mm/yr which is slower than its preferred geologic slip rate at Biskra Palms (14-17 mm/yr) to the south of our location along the fault. This may mean that the slip along this fault has slowed toward north.

In this project, we also tried to assess the reliability of a new OSL approach, dating fanglomerates. Fanglomerates are abundant in fan architectures in arid and semi-arid environments like southern California. Single grain analysis and FMM seem promising in finding the main De population for age assessment. Dose rate heterogeneity in the fanglomerate environment can be tackled by performing ICP-AES/ -MS analysis for <2 mm and >2 mm proportions of the sample and then calculating dose rate based on the weighted mixture. Age of the samples is a critical factor, as small variations in dose rate for older samples will have a less significant effect on the age.

References

Aitken, M., 1985. Thermoluminescence dating: past progress and future trends. Nuclear Tracks and Radiation Measurements 10, 3–6.

Armstrong, P.A., Perez, R., Owen, L.A., Finkel, R.C., 2010. Timing and controls on late Quaternary landscape development along the eastern Sierra El Mayor range front in northern Baja California, Mexico. Geomorphology 114, 415–430.

Auclair, M., Lamothe, M., Huot, S., 2003a. Measurement of anomalous fading for feldspar IRSL using SAR. Radiation measurements 37, 487–492.

Axen, G.J., Fletcher, J.M., 1998. Late Miocene-Pleistocene extensional faulting, northern Gulf of California, Mexico and Salton Trough, California. International Geology Review 40, 217–244.

Balescu, S., Lamothe, M., 1994. Comparison of TL and IRSL age estimates of feldspar coarse grains from waterlain sediments. Quaternary Science Reviews 13, 437–444.

Behr, W., Rood, D., Fletcher, K., Guzman, N., Finkel, R., Hanks, T.C., Hudnut, K., Kendrick, K., Platt, J., Sharp, W., 2010. Uncertainties in slip-rate estimates for the Mission Creek strand of the southern San Andreas fault at Biskra Palms Oasis, southern California. Bulletin 122, 1360–1377.

Bierman, P.R., Montgomery, D.R., 2014. Key concepts in geomorphology. W.H. Freeman and Company.

Blisniuk, K., Oskin, M., Fletcher, K., Rockwell, T., Sharp, W., 2012. Assessing the reliability of U-series and 10Be dating techniques on alluvial fans in the Anza Borrego Desert, California. Quaternary Geochronology 13, 26–41.

Blisniuk, K., Rockwell, T., Owen, L.A., Oskin, M., Lippincott, C., Caffee, M.W., Dortch, J., 2010. Late Quaternary slip rate gradient defined using high-resolution topography and 10Be dating of offset landforms on the southern San Jacinto Fault zone, California. Journal of Geophysical Research: Solid Earth 115.

Blythe, A., Burbank, D., Farley, K., Fielding, E., 2000. Structural and topographic evolution of the central Transverse Ranges, California, from apatite fissiontrack,(U–Th)/He and digital elevation model analyses. Basin Research 12, 97–114.

Bøtter-Jensen, L., Andersen, C., Duller, G.A., Murray, A.S., 2003. Developments in radiation, stimulation and observation facilities in luminescence measurements. Radiation Measurements 37, 535–541.

Bull, W.B., 2000. Correlation of fluvial aggradation events to times of global climate change. Quaternary Geochronology 456–464.

Bull, W.B., 1991. Geomorphic responses to climatic change.

Bull, W.B., 1977. The alluvial-fan environment. Progress in physical geography 1, 222–270.

Burow, C. (2018). calc_CentralDose(): Apply the central age model (CAM) after Galbraith et al. (1999) to a given De distribution. Function version 1.3.2. In: Kreutzer, S., Burow, C., Dietze, M., Fuchs, M.C., Schmidt, C., Fischer, M., Friedrich, J. (2018). Luminescence: Comprehensive Luminescence Dating Data Analysis. R package version 0.8.6. https://CRAN.R-project.org/package=Luminescence

Burow, C. (2018). calc_FiniteMixture(): Apply the finite mixture model (FMM) after Galbraith (2005) to a given De distribution. Function version 0.4. In: Kreutzer, S., Burow, C., Dietze, M., Fuchs, M.C., Schmidt, C., Fischer, M., Friedrich, J. (2018). Luminescence: Comprehensive Luminescence Dating Data Analysis. R package version 0.8.6. https://CRAN.R-project.org/package=Luminescence

Burow, C. (2018). calc_MinDose(): Apply the (un-)logged minimum age model (MAM) after Galbraith et al. (1999) to a given De distribution. Function version 0.4.4. In: Kreutzer, S., Burow, C., Dietze, M., Fuchs, M.C., Schmidt, C., Fischer, M., Friedrich, J. (2018). Luminescence: Comprehensive Luminescence Dating Data Analysis. R package version 0.8.6. https://CRAN.R-project.org/package=Luminescence

Buylaert, J., 2007. Luminescence dating of aeolian sands and silts: a performance study of different techniques and protocols. Doctoral dissertation, Ghent University.

Buylaert, J., Jain, M., Murray, A.S., Thomsen, K.J., Thiel, C., Sohbati, R., 2012. A robust feldspar luminescence dating method for Middle and Late Pleistocene sediments. Boreas 41, 435–451.

Buylaert, J.-P., Murray, A.S., Thomsen, K.J., Jain, M., 2009. Testing the potential of an elevated temperature IRSL signal from K-feldspar. Radiation Measurements 44, 560–565.

Colarossi, D., Duller, G., Roberts, H., Tooth, S., Lyons, R., 2015. Comparison of paired quartz OSL and feldspar post-IR IRSL dose distributions in poorly bleached fluvial sediments from South Africa. Quaternary Geochronology 30, 233–238.

Durcan, J.A., King, G.E., Duller, G.A., 2015. DRAC: Dose Rate and Age Calculator for trapped charge dating. Quaternary Geochronology 28, 54–61.

Duval, M., Campana, I., Guilarte, V., Miguens, L., Iglesias, J., Sierra, S.G., 2015. Assessing the uncertainty on particle size and shape: Implications for ESR and OSL dating of quartz and feldspar grains. Radiation Measurements 81, 116–122.

Fattahi, M., Walker, R., Talebian, M., Sloan, R., Rasheedi, A., 2011. The structure and late Quaternary slip rate of the Rafsanjan strike-slip fault, SE Iran. Geosphere 7, 1159–1174.

Fletcher, K.E., Sharp, W.D., Kendrick, K.J., Behr, W.M., Hudnut, K.W., Hanks, T.C., 2010. 230Th/U dating of a late Pleistocene alluvial fan along the southern San Andreas fault. Bulletin 122, 1347–1359.

Frankel, K.L., Brantley, K.S., Dolan, J.F., Finkel, R.C., Klinger, R.E., Knott, J.R., Machette, M.N., Owen, L.A., Phillips, F.M., Slate, J.L., 2007a. Cosmogenic 10Be and 36Cl geochronology of offset alluvial fans along the northern Death Valley fault zone: Implications for transient strain in the eastern California shear zone. Journal of Geophysical Research: Solid Earth 112.

Frankel, K.L., Dolan, J.F., 2007. Characterizing arid region alluvial fan surface roughness with airborne laser swath mapping digital topographic data. Journal of Geophysical Research: Earth Surface 112.

Frankel, K.L., Dolan, J.F., Finkel, R.C., Owen, L.A., Hoeft, J.S., 2007b. Spatial variations in slip rate along the Death Valley-Fish Lake Valley fault system determined from LiDAR topographic data and cosmogenic 10Be geochronology. Geophysical Research Letters 34.

Galbraith, R.F., 2005. Statistics for fission track analysis. Chapman and Hall/CRC.

Galbraith, R.F., Roberts, R.G., 2012. Statistical aspects of equivalent dose and error calculation and display in OSL dating: an overview and some recommendations. Quaternary Geochronology 11, 1–27.

Galbraith, R.F., Roberts, R.G., Laslett, G.M., Yoshida, H., Olley, J.M., 1999. Optical dating of single and multiple grains of quartz from Jinmium rock shelter, northern Australia: Part I, experimental design and statistical models. Archaeometry 41, 339–364.

Gold, P.O., Behr, W.M., Rood, D., Sharp, W.D., Rockwell, T.K., Kendrick, K., Salin, A., 2015. Holocene geologic slip rate for the Banning strand of the southern San Andreas Fault, southern California. Journal of Geophysical Research: Solid Earth 120, 5639–5663.

Gray, H.J., Owen, L.A., Dietsch, C., Beck, R.A., Caffee, M.A., Finkel, R.C., Mahan, S.A., 2014. Quaternary landscape development, alluvial fan chronology and erosion of the Mecca Hills at the southern end of the San Andreas fault zone. Quaternary Science Reviews 105, 66–85.

Guérin, G., Mercier, N., Nathan, R., Adamiec, G., Lefrais, Y., 2012. On the use of the infinite matrix assumption and associated concepts: a critical review. Radiation Measurements 47, 778–785.

Gurrola, L.D., Keller, E.A., Chen, J.H., Owen, L.A., Spencer, J.Q., 2014. Tectonic geomorphology of marine terraces: Santa Barbara fold belt, California. GSA Bulletin 126, 219–233.

Harvey, A.M., Wigand, P.E., Wells, S.G., 1999. Response of alluvial fan systems to the late Pleistocene to Holocene climatic transition: contrasts between the margins of pluvial Lakes Lahontan and Mojave, Nevada and California, USA. Catena 36, 255–281.

Heermance, R.V., Yule, J.D., 2017. Holocene slip rates along the San Andreas Fault System in the San Gorgonio Pass and implications for large earthquakes in southern California. Geophysical Research Letters.

Huntley, D., Lian, O.B., 1999. Using optical dating to determine when a sediment was last exposed to sunlight. Holocene Climate and Environmental Change in the Palliser Triangle: A Geoscientific Context for Evaluating the Impacts of Climate Change on the Southern Canadian Prairies. Geological Survey of Canada, Ottawa, Bulletin 534, 211–222.

Huntley, D.J., Baril, M., 1997. The K content of the K-feldspars being measured in optical dating or in thermoluminescence dating. Ancient Tl 15, 11–13.

Huntley, D.J., Godfrey-Smith, D.I., Thewalt, M.L., 1985. Optical dating of sediments. Nature 313, 105–107.

Huntley, D.J., Lamothe, M., 2001. Ubiquity of anomalous fading in K-feldspars and the measurement and correction for it in optical dating. Canadian Journal of Earth Sciences 38, 1093–1106.

Jones, L.M., Hutton, L.K., Given, D.D., Allen, C.R., 1986. The July 1986 North Palm Springs, California, Earthquake-The North Palm Springs, California, Earthquake Sequence of July 1986. Bulletin of the Seismological Society of America 76, 1830–1837.

Lamothe, M., Auclair, M., Hamzaoui, C., Huot, S., 2003. Towards a prediction of long-term anomalous fading of feldspar IRSL. Radiation Measurements 37, 493–498.

Lawson, M.J., Roder, B.J., Stang, D.M., Rhodes, E.J., 2012. OSL and IRSL characteristics of quartz and feldspar from southern California, USA. Radiation Measurements 47, 830–836.

Lecce, S.A., 1990. The alluvial fan problem. Alluvial fans: a field approach 3, 24.

Lee, J., Spencer, J., Owen, L., 2001. Holocene slip rates along the Owens Valley fault, California: Implications for the recent evolution of the Eastern California Shear Zone. Geology 29, 819–822.

Li, B., Jacobs, Z., Roberts, R.G., Li, S.-H., 2014. Review and assessment of the potential of post-IR IRSL dating methods to circumvent the problem of anomalous fading in feldspar luminescence. Geochronometria 41, 178–201.

Li, S.-H., Chen, Y.-Y., Li, B., Sun, J., Yang, L.-R., 2007. OSL dating of sediments from deserts in northern China. Quaternary Geochronology 2, 23–28.

Liritzis, I., Stamoulis, K., Papachristodoulou, C., Ioannides, K., 2013. A re-evaluation of radiation dose-rate conversion factors. Mediterr. Archaeol. Archaeom 13, 1–15.

Lisiecki, L.E., Raymo, M.E., 2005. A Pliocene-Pleistocene stack of 57 globally distributed benthic δ18O records. Paleoceanography 20.

McDonald, E.V., McFadden, L.D., Wells, S.G., Enzel, Y., Lancaster, N., 2003. Regional response of alluvial fans to the Pleistocene-Holocene climatic transition, Mojave Desert, California. SPECIAL PAPERS-GEOLOGICAL SOCIETY OF AMERICA 189–206.

McGill, S.F., Owen, L.A., Weldon, R.J., Kendrick, K.J., 2013. Latest Pleistocene and Holocene slip rate for the San Bernardino strand of the San Andreas fault, Plunge Creek, Southern California: Implications for strain partitioning within the southern San Andreas fault system for the last∼ 35 ky. Bulletin 125, 48–72.

McGill, S.F., Spinler, J.C., McGill, J.D., Bennett, R.A., Floyd, M.A., Fryxell, J.E., Funning, G.J., 2015. Kinematic modeling of fault slip rates using new geodetic velocities from a transect across the Pacific-North America plate boundary through the San Bernardino Mountains, California. Journal of Geophysical Research: Solid Earth 120, 2772–2793.

Miller, D.M., Schmidt, K.M., Mahan, S.A., McGeehin, J.P., Owen, L.A., Barron, J.A., Lehmkuhl, F., Löhrer, R., 2010. Holocene landscape response to seasonality of storms in the Mojave Desert. Quaternary International 215, 45–61.

Murray, A.S., Olley, J.M., 2002. Precision and accuracy in the optically stimulated luminescence dating of sedimentary quartz: a status review. Geochronometria 21, 1–16.

Murray, A.S., Schmidt, E., Stevens, T., Buylaert, J.-P., Marković, S., Tsukamoto, S., Frechen, M., 2014. Dating Middle Pleistocene loess from Stari Slankamen (Vojvodina, Serbia)—Limitations imposed by the saturation behaviour of an elevated temperature IRSL signal. Catena 117, 34–42.

Murray, A.S., Wintle, A.G., 2003. The single aliquot regenerative dose protocol: potential for improvements in reliability. Radiation measurements 37, 377–381.

Murray, A.S., Wintle, A.G., 2000. Luminescence dating of quartz using an improved single-aliquot regenerative-dose protocol. Radiation measurements 32, 57–73.

Owen, L., Windley, B., Cunningham, W., Badamgarav, J., Dorjnamjaa, D., 1997. Quaternary alluvial fans in the Gobi of southern Mongolia: evidence for neotectonics and climate change. Journal of Quaternary Science: Published for the Quaternary Research Association 12, 239–252.

Owen, L.A., Clemmens, S.J., Finkel, R.C., Gray, H., 2014. Late Quaternary alluvial fans at the eastern end of the San Bernardino Mountains, Southern California. Quaternary Science Reviews 87, 114–134.

Owen, L.A., Finkel, R.C., Haizhou, M., Barnard, P.L., 2006. Late Quaternary landscape evolution in the Kunlun Mountains and Qaidam Basin, Northern Tibet: a framework for examining the links between glaciation, lake level changes and alluvial fan formation. Quaternary International 154, 73–86.

Owen, L.A., Finkel, R.C., Minnich, R.A., Perez, A.E., 2003. Extreme southwestern margin of late Quaternary glaciation in North America: Timing and controls. Geology 31, 729–732.

Owen, L.A., Frankel, K.L., Knott, J.R., Reynhout, S., Finkel, R.C., Dolan, J.F., Lee, J., 2011. Beryllium-10 terrestrial cosmogenic nuclide surface exposure dating of Quaternary landforms in Death Valley. Geomorphology 125, 541–557.

Ponti, D.J., 1985. The Quaternary alluvial sequence of the Antelope Valley, California. Geol. Soc. Am. Spec. Pap 203, 79–96.

Poolton, N., Ozanyan, K., Wallinga, J., Murray, A., Bøtter-Jensen, L., 2002. Electrons in feldspar II: a consideration of the influence of conduction band-tail states on luminescence processes. Physics and Chemistry of Minerals 29, 217–225.

Prescott, J.R., Hutton, J.T., 1994. Cosmic ray contributions to dose rates for luminescence and ESR dating: large depths and long-term time variations. Radiation measurements 23, 497–500.

Pye, K., Stokes, S., Neal, A., 1995. Optical dating of aeolian sediments from the Sefton coast, northwest England. Proceedings of the Geologists' Association 106, 281–292.

Quigley, M., Sandiford, M., Cupper, M., 2007. Distinguishing tectonic from climatic controls on range-front sedimentation. Basin Research 19, 491–505.

Reheis, M.C., Slate, J.L., Throckmorton, C.K., McGeehin, J.P., Sarna-Wojcicki, A.M., Dengler, L., 1996. Late Quaternary sedimentation on the Leidy Creek fan, Nevada–California: geomorphic responses to climate change. Basin Research 8, 279–299.

Rhodes, E.J., 2015. Dating sediments using potassium feldspar single-grain IRSL: initial methodological considerations. Quaternary International 362, 14–22.

Rittase, W.M., Kirby, E., McDonald, E., Walker, J.D., Gosse, J., Spencer, J.Q., Herrs, A., 2014. Temporal variations in Holocene slip rate along the central Garlock fault, Pilot Knob Valley, California. Lithosphere 6, 48–58.

Rittenour, T.M., 2008. Luminescence dating of fluvial deposits: applications to geomorphic, palaeoseismic and archaeological research. Boreas 37, 613–635.

Ritter, J., Miller, J., Enzel, Y., Howes, S., Nadon, G., Grubb, M., Hoover, K., Olsen, T., Reneau, S., Sack, D., 1993. Quaternary evolution of Cedar Creek alluvial fan, Montana. Geomorphology 8, 287–304.

Ritter, J.B., Miller, J.R., Enzel, Y., Wells, S.G., 1995. Reconciling the roles of tectonism and climate in Quaternary alluvial fan evolution. Geology 23, 245–248.

Robinson, R., Spencer, J., Strecker, M., Richter, A., Alonso, R., 2005. Luminescence dating of alluvial fans in intramontane basins of NW Argentina. Geological Society, London, Special Publications 251, 153–168.

Rockwell, T., Scharer, K.M., Dawson, T.E., 2016. Earthquake geology and paleoseismology of major strands of the San Andreas fault system: Chapter 38.

Roder, B., Lawson, M., Rhodes, E.J., Dolan, J., McAuliffe, L., McGill, S., 2012. Assessing the potential of luminescence dating for fault slip rate studies on the Garlock fault, Mojave Desert, California, USA. Quaternary Geochronology 10, 285–290.

Roozeboom, J.E., 2015. Exploration and application of post-infrared high-temperature infrared stimulated luminescence dating techniques: investigation of marine terrace deposits along the northern San Andreas Fault. Master's thesis, Kansas State University.

Schildgen, T.F., Robinson, R.A., Savi, S., Phillips, W.M., Spencer, J.Q., Bookhagen, B., Scherler, D., Tofelde, S., Alonso, R.N., Kubik, P.W., 2016. Landscape response to late Pleistocene climate change in NW Argentina: Sediment flux modulated by basin geometry and connectivity. Journal of Geophysical Research: Earth Surface 121, 392–414.

Schwartz, G., 1978. Estimating the dimensions of a model. Annals of Statistics 6, 461–464.

Sharp, R.P., Allen, C.R., Meier, M.F., 1959. Pleistocene glaciers on southern California mountains. American Journal of Science 257, 81–94.

Sohbati, R., Murray, A.S., Buylaert, J., Ortuño, M., Cunha, P.P., Masana, E., 2012. Luminescence dating of P leistocene alluvial sediments affected by the A lhama de M urcia fault (eastern B etics, S pain)–a comparison between OSL, IRSL and post-IR IRSL ages. Boreas 41, 250–262.

Spelz, R.M., Fletcher, J.M., Owen, L.A., Caffee, M.W., 2008. Quaternary alluvial-fan development, climate and morphologic dating of fault scarps in Laguna Salada, Baja California, Mexico. Geomorphology 102, 578–594.

Spencer, J.Q., Hadizadeh, J., Gratier, J.-P., Doan, M.-L., 2012. Dating deep? Luminescence studies of fault gouge from the San Andreas Fault zone 2.6 km beneath Earth's surface. Quaternary Geochronology 10, 280–284.

Spencer, J.Q., Oviatt, C.G., Pathak, M. and Fan, Y., 2015. Testing and refining the timing of hydrologic evolution during the latest Pleistocene regressive phase of Lake Bonneville. *Quaternary international*, *362*, pp.139-145.

Spencer, J.Q., Robinson, R.A., 2008. Dating intramontane alluvial deposits from NW Argentina using luminescence techniques: Problems and potential. Geomorphology 93, 144–155.

Spooner, N., 1992. Optical dating: preliminary results on the anomalous fading of luminescence from feldspars. Quaternary Science Reviews 11, 139–145.

Spooner, N.A., 1994. The anomalous fading of infrared-stimulated luminescence from feldspars. Radiation Measurements 23, 625–632.

Spotila, J.A., House, M.A., Niemi, N.A., Brady, R.C., Oskin, M., Buscher, J.T., 2007. Patterns of bedrock uplift along the San Andreas fault and implications for mechanisms of transpression. Geological Society of America Special Papers 434, 15–33.

Stevens, T., Marković, S.B., Zech, M., Hambach, U., Sümegi, P., 2011. Dust deposition and climate in the Carpathian Basin over an independently dated last glacial–interglacial cycle. Quaternary Science Reviews 30, 662–681.

Sylvester, A.G., Smith, R.R., 1976. Tectonic transpression and basement-controlled deformation in San Andreas fault zone, Salton Trough, California. AAPG Bulletin 60, 2081–2102.

Thiel, C., Buylaert, J.-P., Murray, A., Terhorst, B., Hofer, I., Tsukamoto, S., Frechen, M., 2011. Luminescence dating of the Stratzing loess profile (Austria)–Testing the potential of an elevated temperature post-IR IRSL protocol. Quaternary International 234, 23–31.

Thomsen, K., Murray, A., Jain, M., 2011. Stability of IRSL signals from sedimentary K-feldspar samples. Geochronometria 38, 1–13.

Thomsen, K.J., Murray, A.S., Jain, M., Bøtter-Jensen, L., 2008. Laboratory fading rates of various luminescence signals from feldspar-rich sediment extracts. Radiation measurements 43, 1474–1486.

Truelsen, J.L., Wallinga, J., 2003. Zeroing of the OSL signal as a function of grain size: investigating bleaching and thermal transfer for a young fluvial sample. Geochronometria 22, e8.

Van Der Woerd, J., Klinger, Y., Sieh, K., Tapponnier, P., Ryerson, F.J., Mériaux, A., 2006. Long-term slip rate of the southern San Andreas fault from 10Be-26Al surface exposure dating of an offset alluvial fan. Journal of Geophysical Research: Solid Earth 111.

Visocekas, R., 1985. Tunnelling radiative recombination in labradorite: its association with anomalous fading of thermoluminescence. Nuclear Tracks and Radiation Measurements (1982) 10, 521–529.

Visocekas, R., Spooner, N.A., Zink, A., Blanc, P., 1994. Tunnel afterglow, fading and infrared emission in thermoluminescence of feldspars. Radiation Measurements 23, 377–385.

Wallinga, J., Murray, A., Wintle, A., 2000. The single-aliquot regenerative-dose (SAR) protocol applied to coarse-grain feldspar. Radiation Measurements 32, 529–533.

Wells, S.G., McFadden, L.D., Dohrenwend, J.C., 1987. Influence of late Quaternary climatic changes on geomorphic and pedogenic processes on a desert piedmont, eastern Mojave Desert, California. Quaternary Research 27, 130–146.

Wintle, A.G., 2008. Luminescence dating: where it has been and where it is going. Boreas 37, 471–482.

Wintle, A.G., 1973. Anomalous fading of thermo-luminescence in mineral samples. Nature 245, 143.

Wintle, A.G., Murray, A.S., 2006. A review of quartz optically stimulated luminescence characteristics and their relevance in single-aliquot regeneration dating protocols. Radiation measurements 41, 369–391.

Yi, S., Buylaert, J.-P., Murray, A.S., Lu, H., Thiel, C., Zeng, L., 2016. A detailed post-IR IRSL dating study of the Niuyangzigou loess site in northeastern China. Boreas 45, 644–657. https://doi.org/10.1111/bor.12185

Appendix A - pIRIR$_{225}$ KDE and Radial Plots

Post IR-IRSL KDE diagrams and radial plots (plotted in R) are presented in this appendix for all twelve samples. In KDE diagrams, the boxplot shows the distribution parameters: median as bold line, box delimited by the first and third quartile and whiskers defined by the outliers. In radial plots n shows the total number of aliquots, and the gray band represents 2σ.

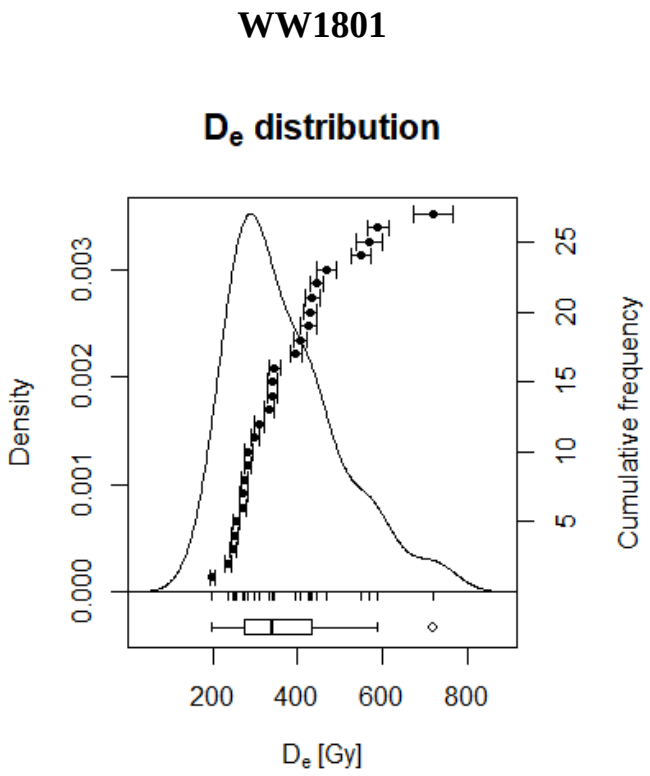

Figure A.1 WW1801 KDE diagram.

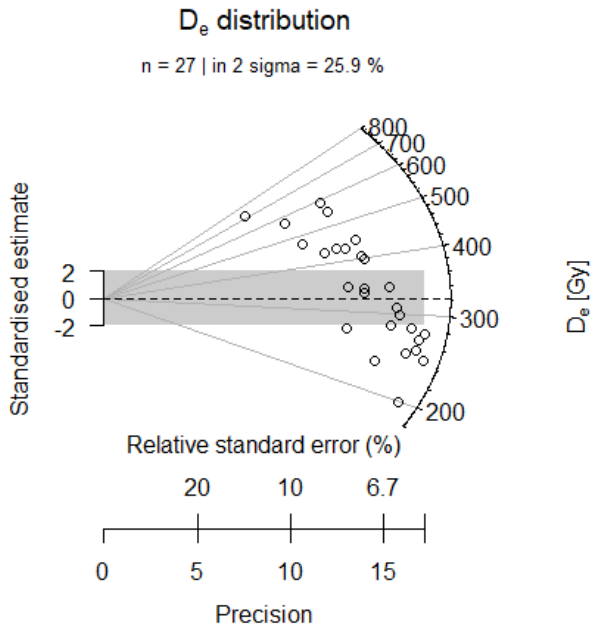

Figure A.2 WW1801 radial plot.

WW1802

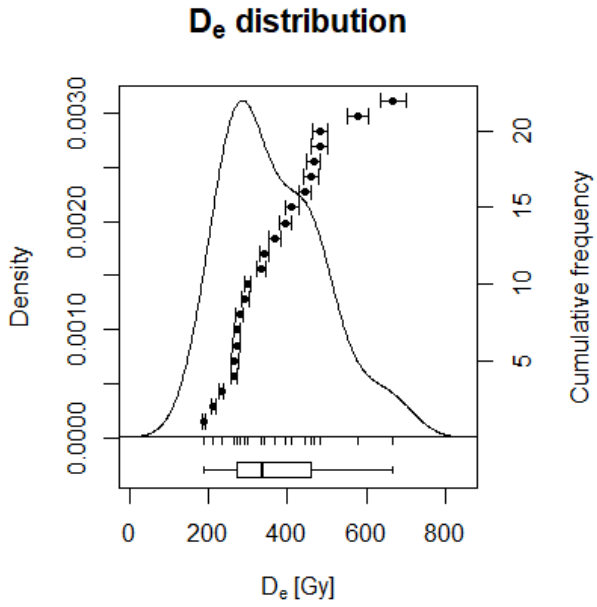

Figure A.3 WW1802 KDE diagram.

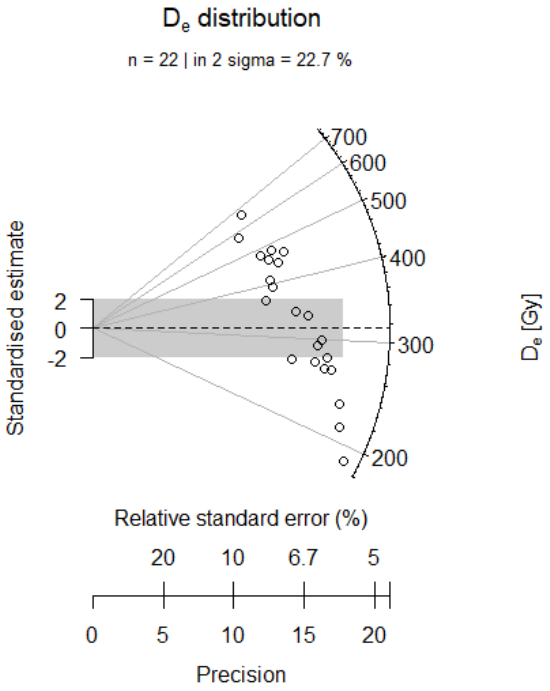

Figure A.4 WW1802 radial plot.

WW1803

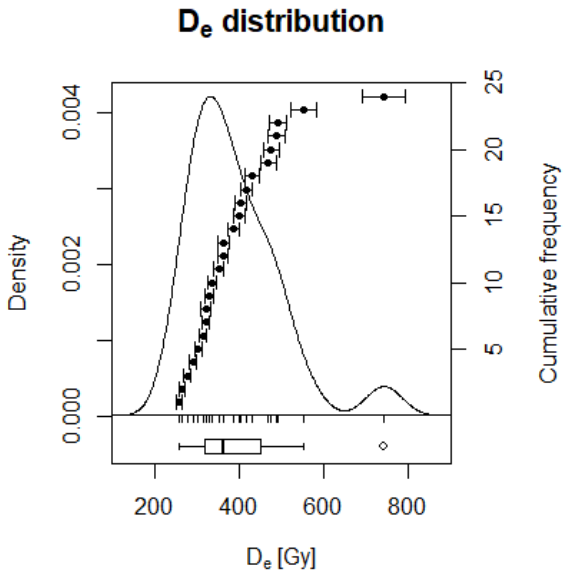

Figure A.5 WW1803 KDE diagram.

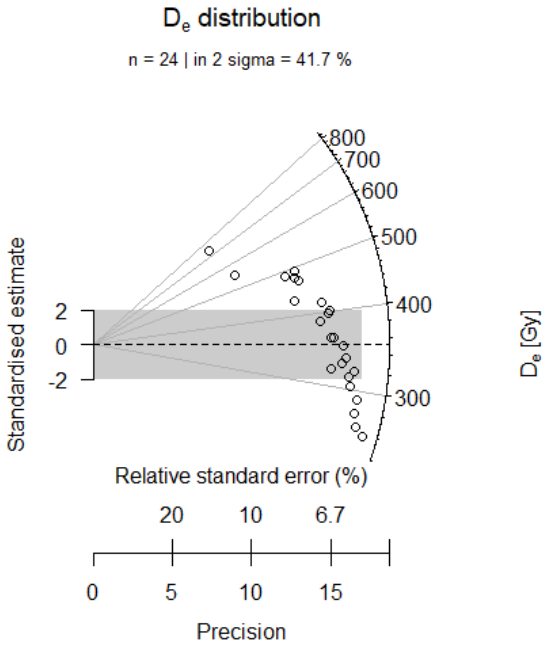

Figure A.6 WW1803 radial plot.

WW1804

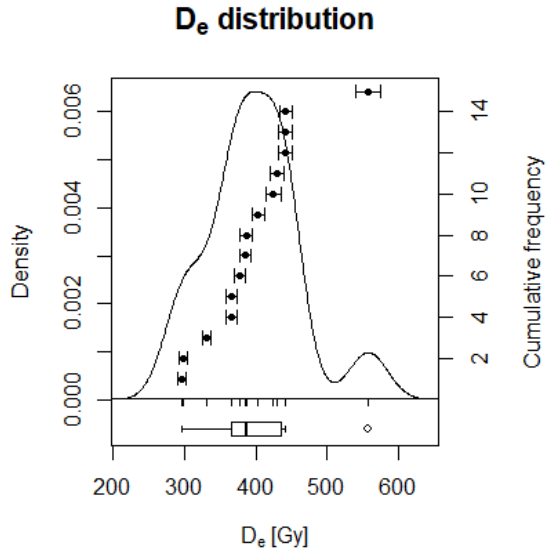

Figure A.7 WW1804 KDE diagram.

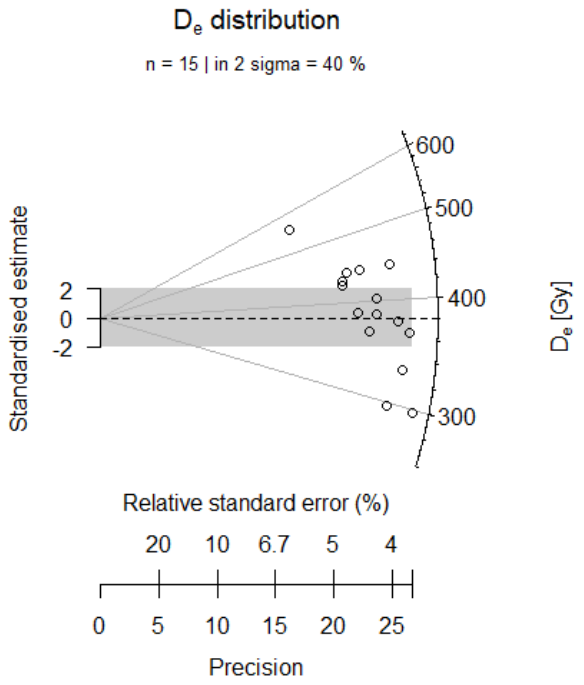

Figure A.8 WW1804 radial plot.

WW1805

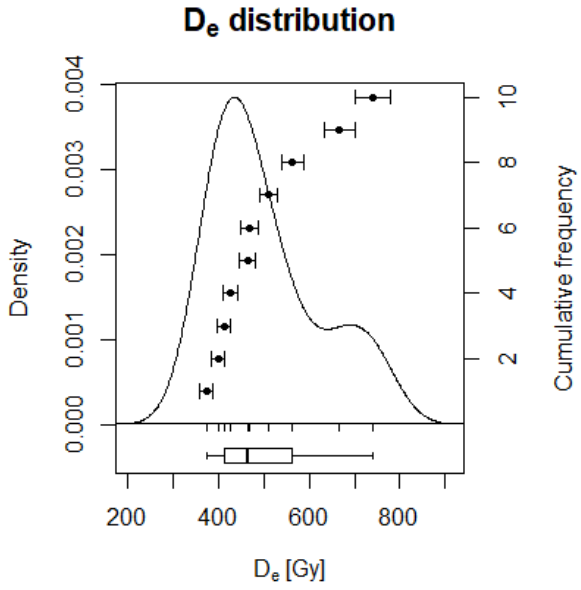

Figure A.9 WW1805 KDE diagram.

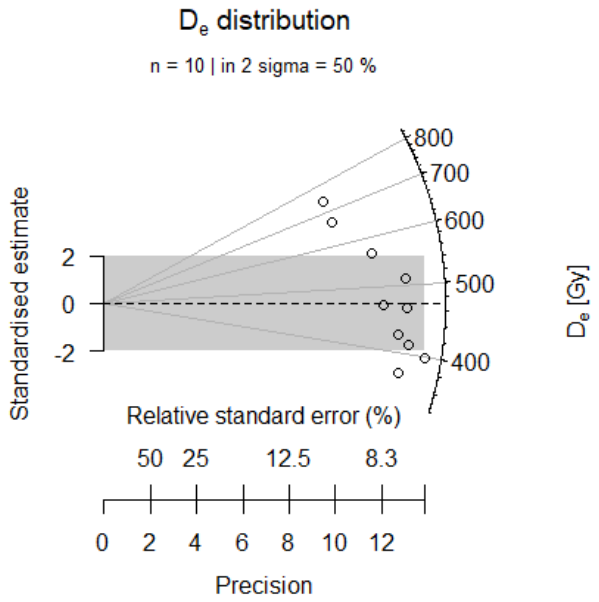

Figure A.10 WW1805 radial plot.

MC1801

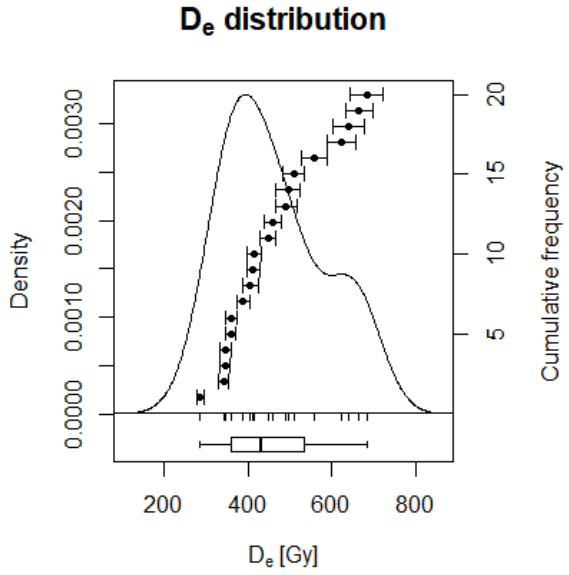

Figure A.11 MC1801 KDE diagram.

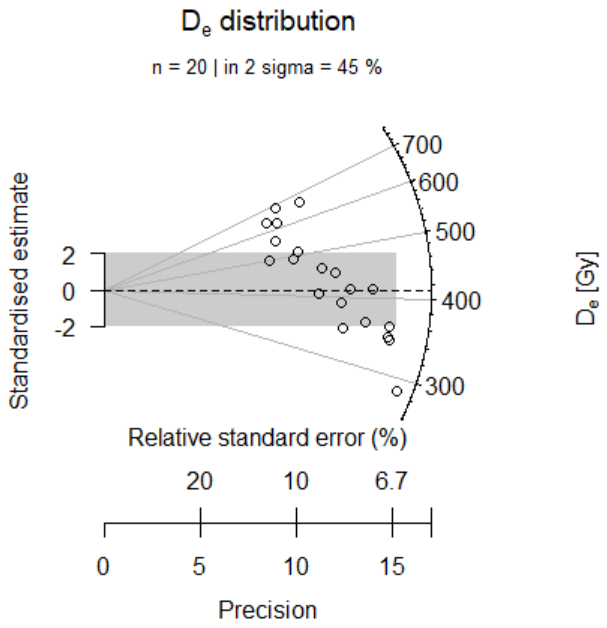

Figure A.12 MC1801 radial plot.

MC1802

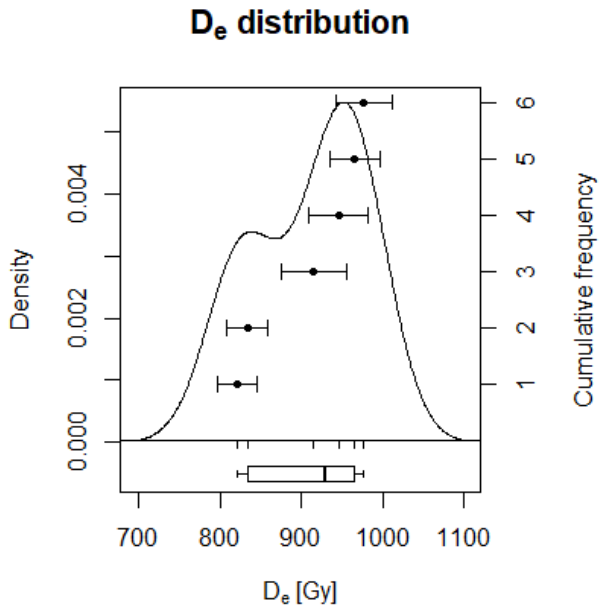

Figure A.13 MC1802 KDE diagram.

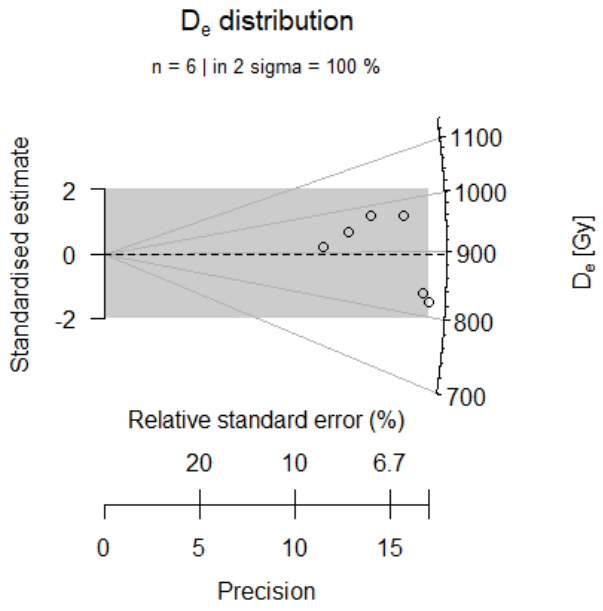

Figure A.14 MC1802 radial plot.

MC1803

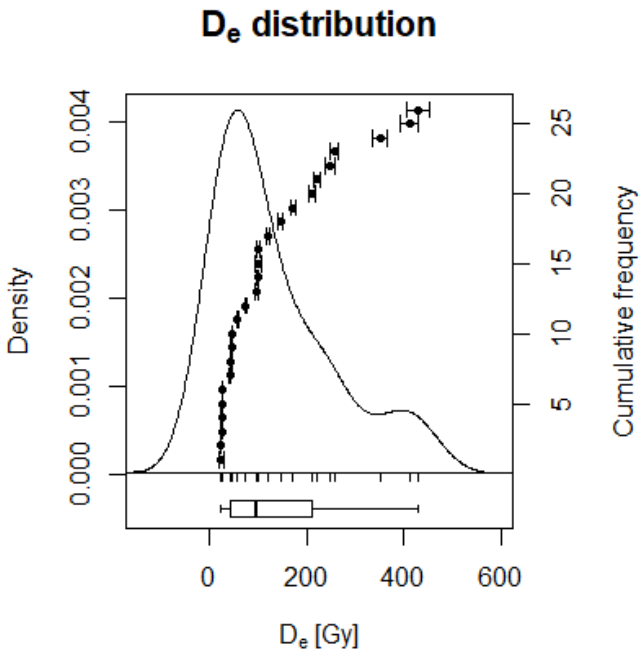

Figure A.15 MC1803 KDE diagram.

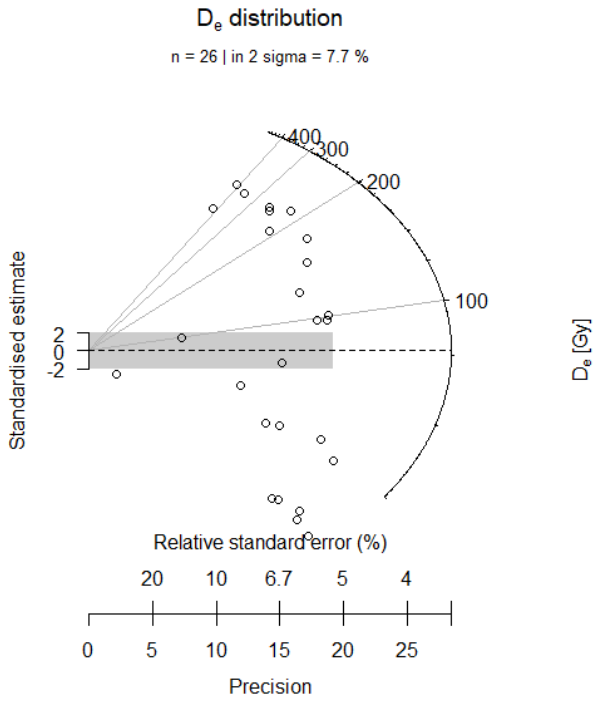

Figure A.16 MC1803 radial plot.

MC1804

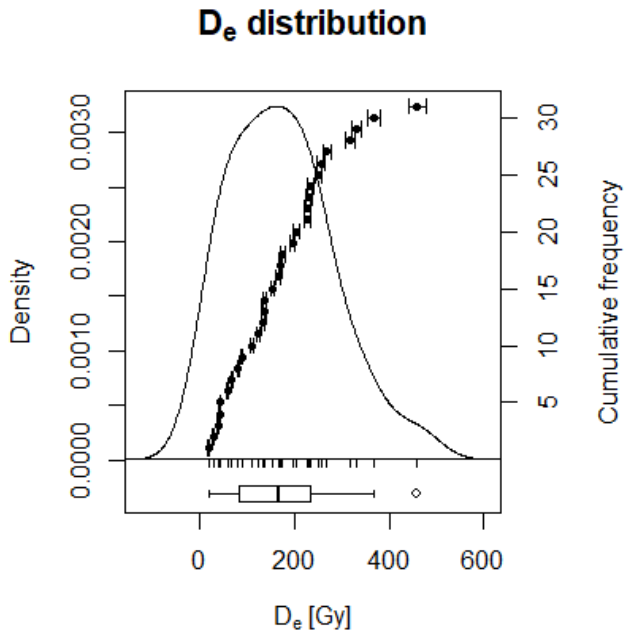

Figure A.17 MC1804 KDE diagram.

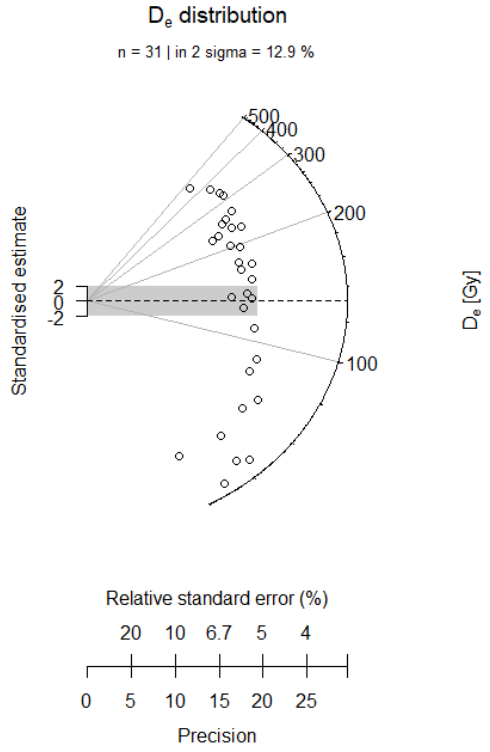

Figure A.18 MC1804 radial plot.

MC1805

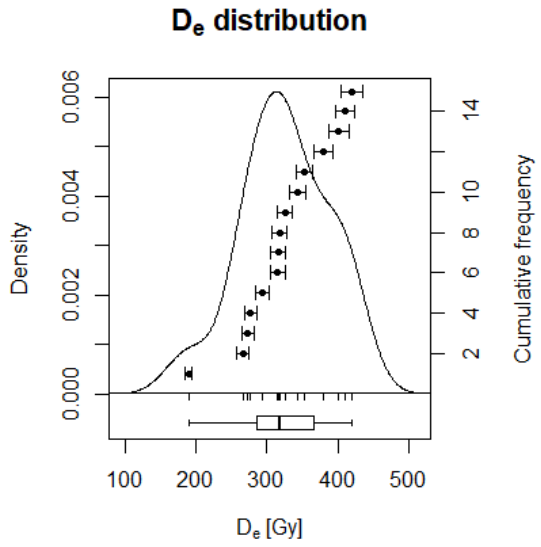

Figure A.19 MC1805 KDE diagram.

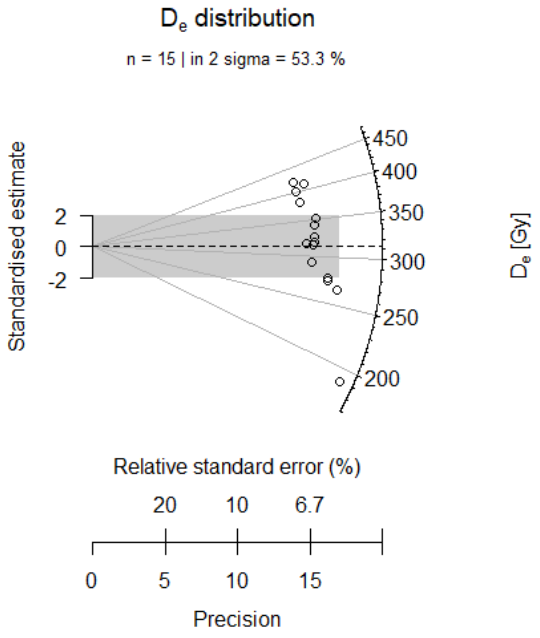

Figure A.20 MC1805 radial plot.

MC1806

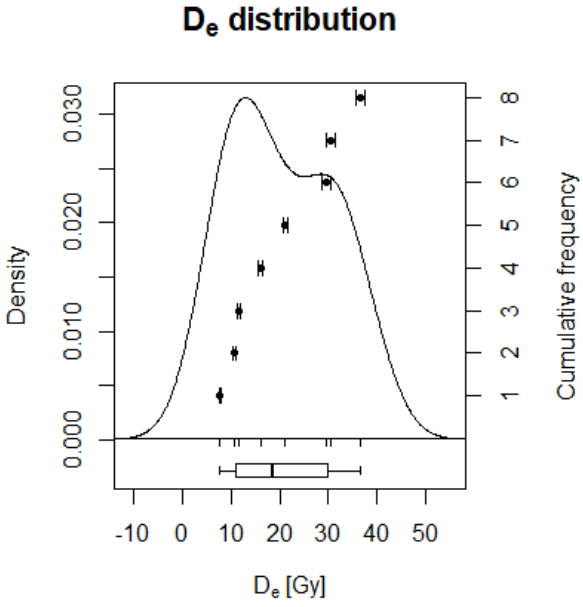

Figure A.21 MC1806 KDE diagram.

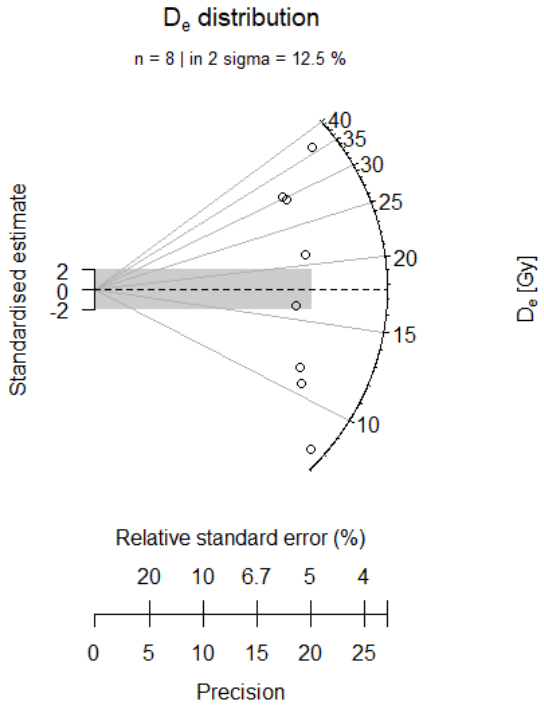

Figure A.22 MC1806 radial plot.

MC1807

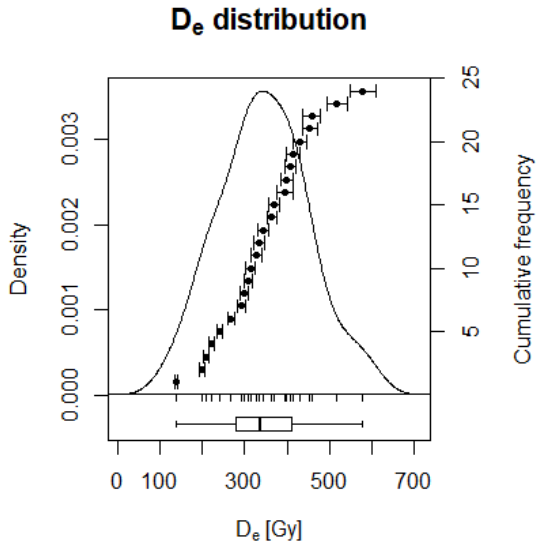

Figure A.23 MC1807 KDE diagram.

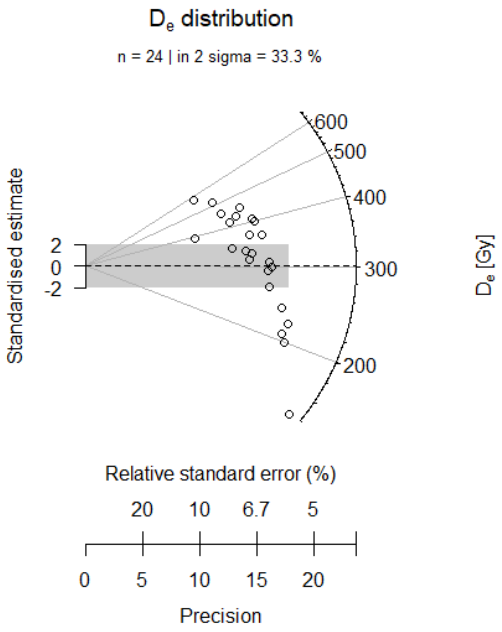

Figure A.24 MC1807 radial plot.

Appendix B - $pIRIR_{225}$ Single Grain Plots

In this appendix KDE diagrams and radial plots for the single grain (SG) analysis of the two fanglomerate samples (WW1803 and MC1807) and WW1801 are presented.

WW1801

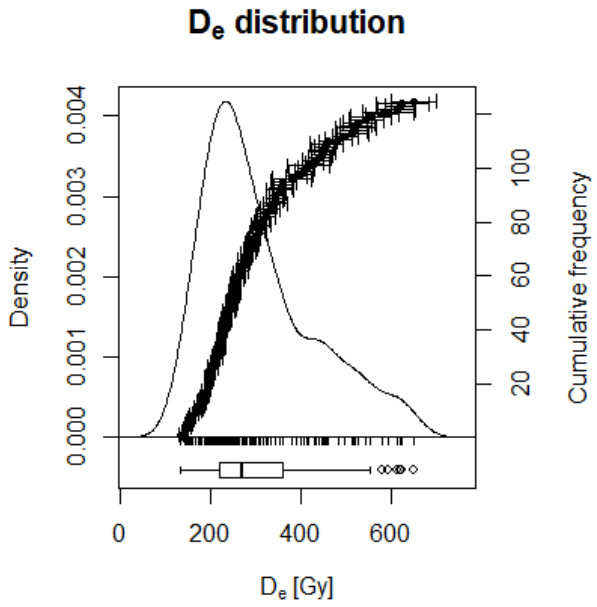

Figure B.1 WW1801 SG KDE diagram.

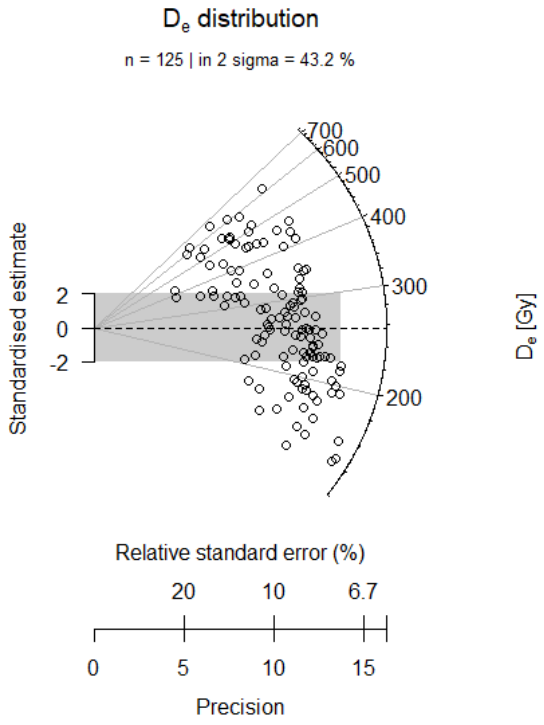

Figure B.2 WW1801 SG radial plot.

WW1803

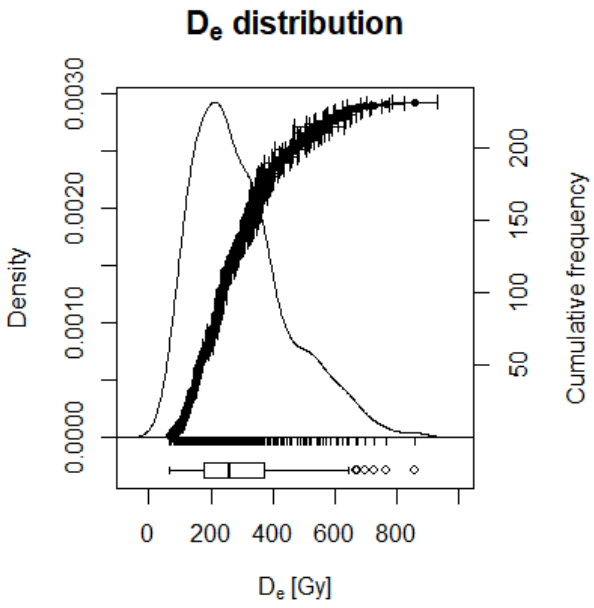

Figure B.3 WW1803 SG KDE diagram.

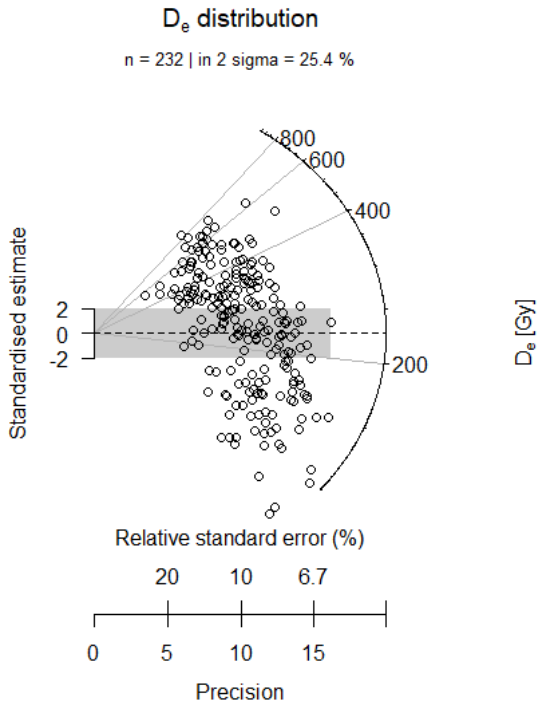

Figure B.4 WW1803 SG radial plot.

MC1807

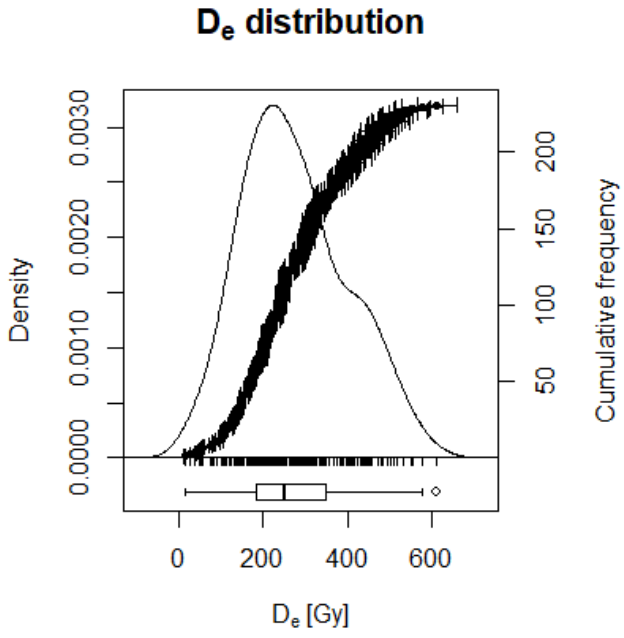

Figure B.5 MC1807 SG KDE diagram.

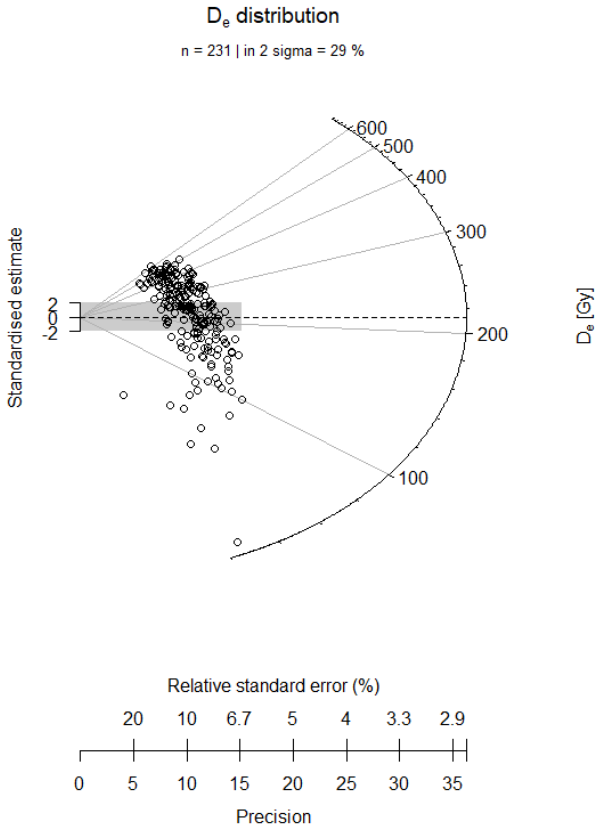

Figure B.6 MC1807 SG radial plot.